



Dália Teresa Al-Alavi Martins

Licenciatura em Engenharia Física

**Compact Ion-source Based on
Superionic Rubidium Silver Iodide
(RbAg₄I₅) Solid Electrolyte**

Dissertação para obtenção do Grau de Mestre em
Engenharia Física

Orientador: Doutor Alexander Borisovich Tolstoguzov

Júri:

Presidente: Prof. Doutor Orlando Manuel Duarte Teodoro

Arguente: Prof. Doutor Reinhard Horst Schwarz

Vogal: Doutor Alexander Borisovich Tolstoguzov

Dália Teresa Al-Alavi Martins

Licenciatura em Engenharia Física

**Compact Ion-source Based on
Superionic Rubidium Silver Iodide
(RbAg₄I₅) Solid Electrolyte**

Dissertação para obtenção do Grau de Mestre em
Engenharia Física

Orientador: Doutor Alexander Borisovich Tolstoguzov

Júri:

Presidente: Prof. Doutor Orlando Manuel Duarte Teodoro
Arguente(s): Prof. Doutor Reinhard Horst Schwarz
Vogal: Doutor Alexander Borisovich Tolstoguzov



Outubro 2013

Compact Ion-source Based on Superionic Rubidium Silver Iodide (RbAg₄I₅) Solid Electrolyte

A Faculdade de Ciências e Tecnologia e a Universidade Nova de Lisboa têm o direito, perpétuo e sem limites geográficos de arquivar e publicar esta dissertação através de exemplares impressos reproduzidos em papel ou de forma digital, ou por qualquer outro meio conhecido ou que venha a ser inventado; e de divulgar através de repositórios científicos e de admitir a sua cópia e distribuição com objetivos educacionais ou de investigação, não comerciais, desde que seja dado crédito ao autor e editor.

Acknowledgements

Dr. Alexander Tolstoguzov for all his supervision, advising, support and confidence in the work in which I have been involved. This thesis could not have been completed without his guidance and help.

Professor Orlando for his constant interest, support and encouragement.

Professor Moutinho, Nenad Bundaleski, João and all the members at the Surface Analysis Group, CEFITEC (Centre of Physics and Technological Research), for their suggestions, questions and encouragement.

Professor Estrela at Chemistry Department, FCUL, for the dozens of XRD analysis, for all her help, patience, time, sympathy and for being a truly inspiring person.

Stefano Caporali, Chemistry Department, University of Firenze, Italia, for the preparation of the first set of micro-probes.

Sónia dos Santos Pereira at CENIMAT for her assistance during thermal evaporation and for performing the thickness measurements.

Tito Busani at CENIMAT for his interest in this project, for his advices and efforts to find the best solution for the deposition.

Manoj Bhanudas Gawande, Pós-Doc Research at the Chemistry Department, FCT-UNL, for preparing the electro-polishing solution for the silver micro-probes.

Professor Rui Lobo, FCT-UNL, for being available to discuss the results of electro-polishing, as well as for sharing his experience and knowledge on similar techniques used in AFM tips.

Mr. Faustino for the mechanical polishing of the micro-probes.

My dear parents and my beloved fiancé, for being part of me.

My dear six-year-old sister, for her surprising interest on ionic currents and experimental work and for having millions of amazing ideas and astonishing questions.

Ana Colaço for her friendship through the last five years.

All Alamas in my residence for their incredible friendship, support, encouragement, interest, companionship and patience.

Ahmed T. E. G. for all the help.

Last but not least, I. H. S. for everything.

Abstract

A compact ion-beam source based on rubidium silver iodide (RbAg_4I_5) solid electrolyte, deposited on a sharpened silver tip, has been developed and studied. Through an accelerating potential above 10 kV, established between emitter and collector, silver positive ions move through the electrolyte towards the emitting surface, where they are emitted from and accelerated. Via partial redox reaction occurring at the silver/ RbAg_4I_5 interface, silver atoms are oxidised into Ag^+ ions and migrate into the electrolyte, compensating the loss of emitted ions in the apex region. The emitted ions are collected by a Faraday cup, producing an electric current in the level of tens picoamperes. It was found that silver ions (atomic or clustered) make a major contribution to the measured ion current, although rubidium ions were also detected with concentration in six times lower than silver.

The apex diameters of the final emitters were estimated in the range of 4-9 μm . The highest stable current was produced by an emitter whose apex diameter corresponds to 8.2 ± 0.5 μm . This current remained in the level of 20-25 pA for nearly 90 minutes and it was obtained at 92°C , using an extraction voltage of 20 kV. Furthermore, it was observed that the current increased exponentially with temperature and linearly with applied voltage, at least for temperatures below 150°C and voltages in the range of 10-22 kV. Dependence on the apex diameter was not studied, since the RbAg_4I_5 film deposited on silver tips was not totally uniform.

Several improvements should be performed to optimize the deposition methods, the design of heating system and methodology of the measurements (m/z characterization of the emitted particles). However, the developed ion-beam source can produce a stable current over a long period of time with minimal expenditure of energy and source material. Such sources have potential applications in materials science and spacecraft engineering as principal elements of miniaturized electric propulsion systems (ionic thrusters).

Keywords: Ionic conductivity, solid electrolyte, RbAg_4I_5 , emitter, ionic current, ion beam

Resumo

Foi desenvolvida e estudada uma fonte de iões compacta baseada na deposição do eletrólito sólido RbAg_4I_5 sobre reservatórios de prata em forma de *tip*. Aplicando uma diferença de potencial superior a 10kV entre o emissor e o coletor, os iões de prata positivos deslocam-se no interior do eletrólito em direção à sua superfície, de onde são emitidos e acelerados. Através de uma reação *redox* parcial na interface $\text{Ag/RbAg}_4\text{I}_5$, os átomos de prata no reservatório são oxidados em iões Ag^+ que migram para o interior do eletrólito, compensando a perda de iões emitidos no extremo do emissor. Os iões emitidos são captados por um coletor do tipo *Faraday cup*, produzindo uma corrente elétrica ao nível das dezenas de pico-amperes. Foi demonstrado que os iões de prata (na forma atômica ou em agregados) são o principal constituinte da corrente medida, embora também possam ser encontrados iões de rubídio numa concentração cerca de 6.6 vezes inferior à da prata.

O diâmetro da extremidade dos emissores finais foi estimado entre 4 e 9 μm . A corrente estável mais elevada foi produzida por um emissor com diâmetro de $8.2 \pm 0.5 \mu\text{m}$ na extremidade. Esta corrente permaneceu entre 20 e 25 pA durante cerca de 90 minutos e foi obtida a 92°C, utilizando uma tensão de extração de 20 kV. Adicionalmente, observou-se que a corrente aumentou exponencialmente com a temperatura e linearmente com a diferença de potencial aplicada, pelo menos para temperaturas inferiores a 150 °C e diferenças de potencial entre 20 e 22 kV. A sua variação com o diâmetro da extremidade do emissor não foi estudada, uma vez que o filme de RbAg_4I_5 depositado sobre os *tips* de prata não foi completamente uniforme.

Diversos melhoramentos poderão ainda ser realizados de forma a otimizar os métodos de deposição, o design do sistema de aquecimento e a metodologia de medição (caracterização massa/carga das partículas emitidas). Contudo, a fonte de iões desenvolvida produz uma corrente estável durante um longo período de tempo, com um gasto mínimo de energia e material. Este tipo de fontes possui potenciais aplicações na área de ciência dos materiais e de engenharia aeroespacial, como elementos fundamentais na miniaturização de sistemas de propulsão (propulsores iónicos).

Palavras-chave: Condutividade iónica, eletrólito sólido, RbAg_4I_5 , emissor, corrente iónica, feixe de iões

Contents

Acknowledgements	iii
Abstract	v
Resumo.....	vii
Contents.....	ix
Figures Content	xi
Tables	xiii
Acronyms	xv
Chapter 1. Introduction	1
Chapter 2. Some General Aspects of Crystalline Solid Electrolytes.....	5
2.1. Origin and thermodynamics of intrinsic point defects in crystalline solids	5
2.2. Ionic Conductivity.....	7
2.3. General classification of solid electrolytes.....	9
Chapter 3. RbAg₄I₅ Solid Electrolyte.....	11
3.1. Crystalline Structure and Ionic Mobility.....	11
3.2. Synthesis, characterization and deposition processes	14
Chapter 4. Ion Source Based on RbAg₄I₅ Solid Electrolyte.....	17
4.1. Brief description of the emitter system	17
4.2. Oxidation and reduction of Silver Ions	17
4.2.1. An ions source as an electrochemical system	17
4.2.2. Ag/RbAg ₄ I ₅ interface: double layer and pseudocapacitance	19
4.3. Transport of Ag ⁺ ions under an applied voltage.....	22
4.4. Emission of Ag ⁺ ions.....	23
4.2.1. Field Ion Emission	23
4.2.2. Field evaporation escape processes.....	23
Chapter 5. Production and Characterization Techniques and Equipment	25
5.1. Resistive Thermal Evaporation	25
5.2. X-Ray Diffraction Analysis System.....	27
5.3. TOF-SIMS System.....	28
Chapter 6. Electrolyte and Micro-Probes Production	33
6.1. Electrolyte Production.....	33
6.2. Reservoir Production.....	35
6.3. Electrolyte deposition.....	37

Chapter 7. Experimental Set Up	39
7.1. General overview	39
7.2. High voltage DC sources.....	40
7.2.1. Material Description.....	40
7. 2. 2. Faraday Cup and Electrometer	41
7. 2. 3. Pico Technology® acquisition system	42
7. 2. 4. Heating system and thermometer	43
Chapter 8. Experimental Results Analysis	45
8.1. Identification of the ion-beam content	45
8.2. Second set of micro-probes	48
8.2.1. Current-temperature dependence	49
8.2.2. Current-time dependence	50
8.2.3. Current-voltage dependence.....	52
Chapter 9. Conclusions	55
References	57

Figures Content

Figure 1. 1. Schematic drawing of the ion source developed by Escher et al. [19].	3
Figure 2. 1. Schematic illustration of (a) Schottky and (b) Frenkel defects in an ionic crystalline structure[25].	5
Figure 3. 1. Representation of the (a) distorted iodine octahedron around Rb^+ and (b) crystal structure of RbAg_4I_5 , showing the cubic unit cell as the blue-lined box [33]. The larger spheres at right correspond to I^- , medium spheres to Rb^+ and small spheres to Ag^+ .	12
Figure 3. 2. Projection of the crystal structures of (a) $\alpha\text{-RbAg}_4\text{I}_5$ at 295K along the plane [111], (b) $\beta\text{-RbAg}_4\text{I}_5$ at 150K along plane [001] and (c) $\gamma\text{-RbAg}_4\text{I}_5$ at 90 K along the plane [001]. The upper part presents the structures without silver ions and the lower part presents silver ions in a structure where Rb^+ and I^- are downscaled [38].	13
Figure 3. 3. Conductivity of Ag^+ in RbAg_4I_5 in the temperature range 125 K and 1000 K [39].	14
Figure 3. 4. Phase diagram of $\text{RbI}+\text{AgI}$ system [41]. The eutectic point (red colour) occurs at 197°C for a mixture with 30% of RbI .	14
Figure 4. 1. Schematic representation of (a) a simple electrochemical system and (b) the proposed Ag^+ emitter system.	18
Figure 4. 2. Stern model of a general double layer formed in the interface between a positively charged surface and an electrolyte in aqueous solution [44]. Solvated cations migrate and adsorb to the electrolyte surface due to electrostatic forces. Potential drop is represented on the interface.	19
Figure 4. 3. Schematic representation of the emitter system (a) before high voltage is applied and (b) after the double layer is formed at the interface silver/electrolyte, where oxidation of silver atoms takes place.	21
Figure 4.4. Simulation of Ag^+ trajectories using a distance of (a) 5 mm and (b) 1 mm between the micro-probe and collector. Resolution is 0.033(3) mm (i.e., 1mm corresponds to 30 points).	42
Figure 5. 1. Schematic view of resistive thermal evaporation chamber. Typically, a voltage in the range of 6-20V is applied to the electrodes and a current of 50-100A passes through the crucible.	25
Figure 5. 2. Schematics representation of evaporation from a surface source.	26
Figure 5. 3. Thermal resistive evaporation system at CENIMAT.	27
Figure 5. 4. Schematic presentation of X-ray diffraction. The plane [hkl] is perpendicular to the plane of atoms.	27
Figure 5. 5. Philips Analytical PW 3050/60 X'Pert PR diffractometer.	28
Figure 5. 6. Schematic representation of emission of secondary particles initiated by the impact of primary beam [50].	29

Figure 5. 7. ToF-SIMS equipment and its main components.....	31
Figure 6. 1. XRD diffraction patterns of α -RbAg ₄ I ₅ powder. The main peaks corresponding to RbAg ₄ I ₅ are marked with lines and blue points represent peaks, which belong to α -AgI electrolyte.....	34
Figure 6. 2. Schematic drawing of the silver reservoir.	35
Figure 6. 3. XRD diffraction patterns of silver reservoir #4 ($7.8 \pm 0.5 \mu\text{m}$ of diameter). This tip was randomly selected for analysis and the composition of all other reservoirs was assumed to be similar.....	37
Figure 6. 4. Thermal evaporation chamber and details of (a) silver tips in the substrate holder and (b) RbAg ₄ I ₅ powder electrolyte in the crucible before the deposition. From right to left, silver tips ordered from numbers 1 to 4, according to the classification used in Table 2.	38
Figure 7. 1. Overview of the experimental set up. The emitter system is placed in the preparation chamber of ToF-SIMS at 10^{-8} - 10^{-9} mbar.....	39
Figure 7.2. Emitter system (in the centre) and its connections. The small yellow dot is on the region between electrodes, travelled by the emitted particles. 1- High voltage DC source; 2- Electrode holding micro-probe; 3- Faraday Cup; 4- Electrometer; 5- Pico Technology® acquisition data hardware; 6- Computer/ PicoLog® software; 7-Thermometer; 8- Heating system. Ground connections are not shown.	40
Figure 7. 3. High voltage connection to the chamber: (a) without high voltage cable and before mounting the emitter system in the preparation chamber and (b) after that, with high voltage cable and insulation.....	41
Figure 7. 4. Faraday Cup components: (a) inner and outer cylindrical electrodes and (b) cap. Ceramics was used to isolate the collector from the ground.	41
Figure 7. 5. Pico Technology® device for data acquisition.	42
Figure 8. 1. Current-time graph for an emitter composed of silver wire dipped into the melted electrolyte (room temperature, 20 kV of accelerating potential)	46
Figure 8.2 Mass spectrum of positive secondary ions obtained for as-received nickel foil (before being placed inside the Faraday cup).....	47
Figure 8. 3 Mass spectrum obtained from a nickel foil after its exposure to the ion beam emitted from the electrolyte ion-beam source.....	45
Figure 8. 4. Dependence of the ion current on temperature under an accelerating voltage of 20 kV.....	49
Figure 8. 5. Current-time dependence at 92°C obtained using an accelerating voltage of 20 kV.	51
Figure 8. 6. Current-voltage dependence at 77°C and 92°C.....	52

Tables

Table 6. 1. Images of the handcrafted silver reservoirs apexes before and after polishing with sand paper and their estimated diameters..... 36

Table 8. 1. Experimental and corrected ratio of Ag and Rb secondary ion peaks in ToF-SIMS spectrum of the nickel foil..... 47

Acronyms

a	Interatomic space Electric field Kinetic energy
F	Faraday constant ($9.649 \times 10^4 \text{ C mol}^{-1}$)
j	Current density Field evaporation rate Field reduction factor
MAg ₄ I	M silver iodide (M stands for Na, K, Rb, Tl and NH ₄)
MIM	Metal/insulator/metal
m/z	Mass to charge ratio
n_e	Number of electrons
n_s	Number of Schottky defects
n_f	Number of Frenkel defects Number of sites Number of interstitial sites
Na- β -alumina	Sodium beta alumina Net flux density of ions
pA	Picoampere
q	Charge number
R	Apex radius
RbAg ₄ I ₅	Rubidium Silver Iodide Thermal evaporation rate
RSF	Relative Sensitivity Factor
RTE	Resistive Thermal Evaporation
SIMS	Secondary Ion Mass Spectrometry
ToF-SIMS	Time-of-Flight Secondary Ion Mass Spectrometry
XRD	X-Ray Diffraction Analysis Gibb's free energy Wavelength Chemical potential Electrochemical Potential Ionic conductivity

Chapter 1. Introduction

There are two types of conductivity, electronic and electrolytic, and both types can occur in all states of matter. Materials in solid state, which have mainly electrolytic conductivity, through the movement of positive or negative ions, and negligible electronic conductivity are named solid electrolytes. Electrolytes with high values of ionic conductivity (10^{-1} - $10^{-4} \Omega^{-1} \text{ m}^{-1}$) are also referred as superionic or fast ion conductors.

Prior to 1960 most of the devices were based on electron conducting materials, as semiconductors, and very few ion conducting materials were available. In 1967 two different types of electrolytes were revealed: Na- β -alumina, with movable Na^+ ions, found by Yao and Kummer [1], and MAg_4I_5 compounds (M standing for Na, K, Rb, Tl and NH_4), discovered by Bradley and Greene [2, 3] and independently by Owens and Argue [4]. In particular, these MAg_4I_5 compounds presented exceptionally high ionic conductivity and all contained the same movable Ag^+ ion, which do not occupy particular single sites in the crystalline lattice [3]. Since then, several other solid electrolytes with various mobile species have been discovered, namely H^+ , Li^+ , K^+ , Cu^+ , F^- and O_2^- . However, rubidium silver iodide (RbAg_4I_5) solid electrolyte, belonging to MAg_4I_5 compounds, is still the solid electrolyte with the highest known ionic conductivity at room temperature ($0.124 \Omega^{-1} \text{ m}^{-1}$ at 20°C [2]) and has been employed in various technological applications.

Since the 70s, RbAg_4I_5 has been used in solid-state batteries [6], with high faraday efficiency and several advantages in terms of shelf life after ten years [7] and twenty years storage [8]. More recently, Taralunga *et al.* [9] established that an $\text{Ag}/\text{RbAg}_4\text{I}_5/\text{RbI}_3$ battery presents good electrochemical characteristics to be used in cardiac pacemakers and other medical devices.

RbAg_4I_5 has also been used in the field of Nanotechnology, for structuring and modifying nano-devices. As an example, an AFM-aided nanolithography technique was developed based on the high ionic conductivity of Ag^+ ion in RbAg_4I_5 [10]. When a negative voltage is applied on the AFM probe relative to a counter electrode, composed of RbAg_4I_5 thin film on silver, silver atoms at that electrode are electrochemically oxidized into positively charged Ag^+ ions. Then those ions can migrate across the electrolyte to its surface, where they are reduced into Ag atoms directed at the tip, resulting in nano-sized Ag pattern.

Also in nanotechnology applications RbAg_4I_5 was used as a mean to produce silver nanowires [11]. As reported, a crystalline film of RbAg_4I_5 was deposited on a substrate and covered by aluminium thin film in two distinct places, creating two electrodes. At room

conditions and under a potential difference between electrodes, Ag atoms are oxidized in the positive electrode, losing an electron. Ag^+ ions then migrate through the electrolyte towards the cathode, where they are reduced into Ag atoms, which form clusters and grow as wires. By the contrary, reproducing this experiment using silver electrodes instead of the aluminium ones, Ag^+ ions can uninterruptedly migrate through the electrolyte towards the cathode, negatively charged. This continuous migration evidences that positive electrode behaves like a reservoir of silver ions, oxidising silver atoms in the interface silver/electrolyte, and the negative electrode as a consumer of Ag^+ ions, reducing them into silver atoms again.

Others application of RbAg_4I_5 thin films are electric switching devices, transistors and capacitors. Electric switching devices are composed of electrolyte film sandwiched between Ag and Pt electrodes [12]. This sort of devices can be switched between high- and low-resistance states by applying a voltage with opposite polarities, as a consequence of the growth and dissolution of Ag dendrites, also due to oxidation-reduction reactions [13, 14]. A field configurable transistor can be fabricated on a Si nanowire FET (field-effect transistor) platform by integrating a thin film of conjugated polymer and RbAg_4I_5 ionic conductive layer into the gate [15]. In the case of electrochemical capacitors, they consist of capacitors with electrical double layer, considered promising rechargeable current sources [16].

More recently, in the field of atomic manipulation, Valov *et al.* [17] set a potential difference between a scanning tunnelling microscope (STM) tip and the RbAg_4I_5 electrolyte on silver. In this case, Ag^+ ions in the electrolyte were reduced at its surface, forming Ag atoms, and there a nucleus may grow so that a single atomic contact to the STM tip was possible. In the sequence of these results, Valov and Kozicki [18] published a review on the utilization of solid electrolytes as RbAg_4I_5 in cation based switching memory cells. These devices have a metal-insulator/electrolyte-metal (MIM) structure and are also based on cation migration and redox (reduction/oxidation) reactions to form and remove a conducting filament between electrodes (generally made of Ag or Cu). Once formed, the Ag^+/Cu^+ filament bridges the insulator electrolyte and the device is in the low-resistance ON state. Applying a voltage with the opposite polarity, the filament dissolves and the cell returns to the high-resistance OFF state.

More than proving its versatility, the referred technological applications of RbAg_4I_5 demonstrate its potential as an effective solid state mean for the diffusion of silver ions, capable of being reduced or oxidized when silver electrodes are in contact the electrolyte and proper potential difference is set. Besides, thermal evaporation of RbAg_4I_5 was proved to produce crystalline thin films on electrodes.

Thermionic and field ion emission from electrolytes are also topics of interest (see, e.g. [19], [20]) with numerous compounds, both solid and liquid, being studied. The long-term objective of these studies is the development of bright and fine focusable ion beam sources for applications in ion lithography [21], materials analysis, and space propulsion [22].

Considering focused ion beam sources, Escher *et al.* [19] developed a source based on $(\text{AgI})_{0.5}(\text{AgPO}_3)_{0.5}$ amorphous solid electrolyte, containing the same Ag^+ movable ion as in case of RbAg_4I_5 . Under vacuum conditions and by applying a potential difference between a sharpened electrolyte tip and a detector, Ag^+ ions are reported to be field emitted, as represented in Figure 1.1. Since the electrolyte is in contact with a silver reservoir, silver atoms in that interface are oxidized into Ag^+ ions, which then move into electrolyte and replenish those emitted from the apex.

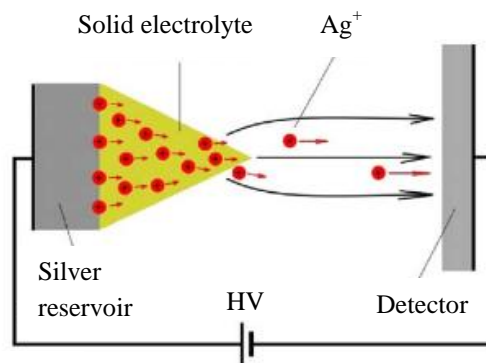


Figure 1. 1. Schematic drawing of the ion source developed by Escher *et al.* [19].

The present work aims to develop an ion source-based on the emission of movable ions from a solid electrolyte, mainly for future applications in innovative solid state ion thrusters for aerospace engineering. Having a simpler and lighter packing, this new type of all solid state thrusters could be able to compete with ion electrospray thrusters, which require the extraction and acceleration of ions from liquids. RbAg_4I_5 solid electrolyte was chosen for this purpose because it has the highest known ionic conductivity at room temperature ($0.124 \Omega^{-1} \text{m}^{-1}$ at 20°C [2]), contains a high mass movable ion (Ag^+) and well known crystalline structure and properties. Of course, this ion source based on RbAg_4I_5 also opens a broad field of applications in general ion-beam sources, nano-devices and surface analysis.

We suggest some improvements in the contact between electrolyte and silver reservoir, relatively to the work of Escher *et al.* [19], where silver and electrolyte were introduced in a glass capillary. For example, tension strings could be used as a means of pressuring the silver reservoir against the electrolyte tip, as suggested in a recent solid state ion beam generator patent [23], whose general configuration is similar to the one in Figure 1.1. However, these extra components and the necessity of adding cases to attach the strings increase the complexity and costs of the emitter system.

While pressing the reservoir and electrolyte surfaces against each other, as made by Taralunga and Rus [9], would be suitable for flat surfaces, the deposition of RbAg_4I_5 on silver

allows the adsorption of the evaporating electrolyte by silver. Physical vapour deposition, usually involving resistive thermal evaporation of the compound, or, more rarely, pulsed laser deposition have already been used to produce RbAg_4I_5 thin films on silver [10, 18]. Both techniques have the advantage of being suitable for non-flat substrates, such as tips or micro-probes.

After some preliminary measurements obtained with silver wires dipped into melted RbAg_4I_5 have confirmed poor adherence between those compounds, resistive thermal evaporation of RbAg_4I_5 was assumed as being the most suitable process to properly join the silver reservoir and the solid electrolyte. Since the high malleability of the silver wire also contributes for the low adherence, silver rods (~1.3 mm of diameter) were sharpened and covered by RbAg_4I_5 thin film. Hence, it was obtained a final micro-probe from where Ag^+ ions are emitted from, under an applied voltage. The dependencies of the ionic current on the temperature and the applied voltage were studied as well as the stability of the current versus time.

The present dissertation contains nine chapters. In Chapter 2 some theoretical aspects on ionic conductivity in crystalline solids are presented as well as its relation with intrinsic defects in the crystalline structure. Some recent classifications of solid electrolytes are included too. Chapter 3 is devoted to RbAg_4I_5 , focusing on the different phase transitions through which RbAg_4I_5 might undergo and their effect on Ag^+ mobility. Some processes recently used for its production and deposition are described as well. In Chapter 4 detailed description of the physical processes of emission of silver ions from the electrolyte and oxidation of silver atoms from the reservoir can be found. Chapter 5 describes the fundamentals of resistive thermal evaporation (RTE), X-rays diffraction analysis (XRD) and time-of-flight secondary ion mass spectrometry (ToF-SIMS). Respectively, these techniques were used to deposit the electrolyte on silver reservoirs, for studying crystalline structure of silver reservoirs, RbAg_4I_5 powder and RbAg_4I_5 thin films, and to identify Ag^+ ions as the main emitted particles from the electrolyte. Chapter 6 describes the production of the emitters and Chapter 7 the experimental set up. Chapter 8 reports the most relevant results and respective analysis. Chapter 9 summarizes the main conclusions and indicates potential areas for further research.

Chapter 2. Some General Aspects of Crystalline Solid Electrolytes

This chapter introduces some theoretical aspects of ionic conductivity in crystalline solids. It includes the origin of intrinsic defects in crystalline structures and their contribution to ionic conductivity, whether interstitial or through sites.

Classification of crystalline ionic conductors and solid electrolytes is also presented.

2.1. Origin and thermodynamics of intrinsic point defects in crystalline solids

At the absolute zero of temperature all ions would be in the respective positions in the lattice, therefore forming a perfect crystal. However, at any non-zero temperature there are always defects in crystalline structures, which usually fall into the following groups:

- point defects: vacancies, interstitials and impurity atoms;
- line defects, such as dislocations;
- planar effects, as grain boundaries;
- volume defects: voids or different phase presence.

Point defects are necessary for ion transport in ionic crystals [5],[24]. These might be formed in elemental or ionic crystals and fall into two main categories: intrinsic defects, if the stoichiometry of the compound is kept, and extrinsic defects, if the defects are created through the introduction of a foreign atom into the lattice.

Intrinsic defects corresponding to Schottky or Frenkel defects are represented in Figure 2. 1. Schottky defects are created when a pair of vacancies originated by single cation and single anion leaving their positions in the crystalline lattice. The creation of a single vacancy due to the wandering of one ion in interstitial sites results in a Frenkel defect.

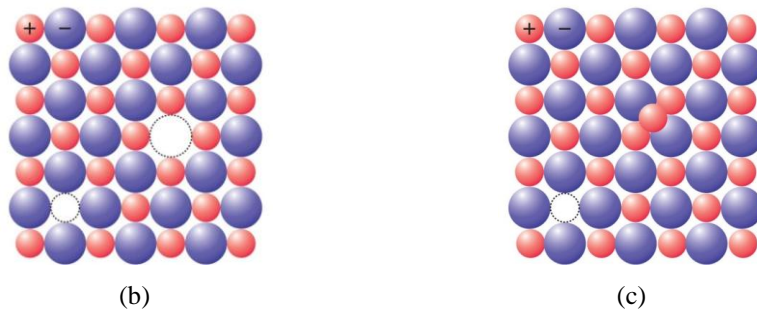


Figure 2. 1. Schematic illustration of (a) Schottky and (b) Frenkel defects in an ionic crystalline structure [25].

The process of formation of intrinsic defects is always endothermic, meaning that energy is required for moving an ion, and the entropy increases as a result of the respective vacancy creation. Thus, the enthalpy of formation of the defects is balanced by the gain in entropy such that at equilibrium the overall change in free energy of the crystal is zero [26], according to the general equation of Gibb's free energy for migration of ions:

where ΔH_f and ΔS_f correspond to the enthalpy and entropy of formation of defects and T to the temperature in Kelvin.

Defects increase in concentration until the free energy reaches its minimum. Hence, in equilibrium, the vacancy concentration can be found through the minimization of the free energy of the crystal. For Schottky defects, Schottky pairs corresponds to an equal amount of anion vacancies, n_{-} , and cation vacancies, n_{+} , considering a 1:1 crystal lattice with N sites. Employing the Boltzmann formula to express the entropy of this system,

where k is the Boltzmann constant and Ω is the number of different ways to randomly distribute Schottky pairs over N sites. Ω is hence equivalent to the product between Ω_{+} ways to randomly distribute cations and Ω_{-} ways to distribute anions. As in an ionic crystal the electrical neutrality is preserved, n_{+} and n_{-} can both expressed by:

$$n_{+} = n_{-} = n_s$$

Rewriting the entropy of the system and the free energy expression, we obtain, respectively:

At the equilibrium the free energy of Gibbs corresponds to the minimum with respect to changes in the number of defects, n_s ,

$$\frac{\partial G}{\partial n_s} = 0$$

and after some manipulation, we obtain:

Finally, using equation (2.1) and considering N as being much higher than n_s , the number of Schottky pairs is:

$$n_s = \sqrt{\frac{N \Delta S_f}{\Delta H_f}}$$

and ΔH_f corresponds to the energy necessary for the creation of one Schottky defect.

Similarly, the number of Frenkel defects can be described by:

$$n_f = \sqrt{\frac{N_i \Delta S_f}{\Delta H_f}}$$

where N_i is the number of interstitial sites.

In conclusion, at any non-zero temperature there are always defects since the amount of defects or increases with the temperature, as it is showed by equations (2.8) and (2.9). At zero temperature Gibb's free energy is dominated by the enthalpy, which has its lowest value, and, by increasing the temperature, the contribution from enthalpy to free energy becomes higher, according to equations and . Hence, the origin of the crystal defects arises from the system attempting to minimize the free energy through an increase in entropy.

2.2. Ionic Conductivity

Considering an ideal crystal, in which all of the constituent ions are arranged in a regular periodic fashion and often stacked in a close-packed form, the interstitial space available for the diffusion of ions might be just enough for the vibration around the equilibrium position. On the contrary, in the case of nearly perfect crystals, the existence of defects in the lattice is responsible for the ionic diffusion or, in other words, for the motion of ionic species through vacancies or interstitial sites. This diffusion of ions across a crystal lattice is the mechanism responsible for the ionic conductivity in solid electrolytes [26] so that the application of an external field creates a net ionic current.

According to the Einstein model, the probability P (per unit of time) for a given ion to jump from one site to another (interstitial or vacancy) is expressed by [27]:

$$P = \nu \exp\left(-\frac{E_a}{kT}\right)$$

where ν represents the frequency of the ions around their mean position in a potential well of barrier height equivalent to E_a , Gibb's free energy for the migration of ions.

Without electric field, an equal number of ions jumps in opposite directions. However, when an external electric field gradient, E , is applied, the jump probability of the ions, with charge q and interatomic space a , in and against the direction of the field, is respectively:

$$P_{\text{forward}} = \nu \exp\left(-\frac{E_a - qEa}{kT}\right)$$

$$P_{\text{backward}} = \nu \exp\left(-\frac{E_a + qEa}{kT}\right)$$

The number of ions per unit of volume moving in the direction of the applied field, n_{net} , among n charge carriers per unit of volume is

and if assumed that $n_{\text{net}} = n(P_{\text{forward}} - P_{\text{backward}})$, equation (2.13) might be rewritten as

$$n_{\text{net}} = n \nu a \exp\left(-\frac{E_a}{kT}\right) \left[\exp\left(\frac{qEa}{kT}\right) - \exp\left(-\frac{qEa}{kT}\right) \right]$$

The current density j corresponds to the number of charge carriers passing through per unit of area per unit of time, as follows,

and the ionic conductivity corresponds to the quotient between equation and the electric field gradient. Hence, we obtain:

Equation (2.17) can be generalized to an Arrhenius-type equation, described by

where stands for the pre-exponential factor, which coincide with and for Schottky and Frenkel defects, respectively, and represents the activation energy of ion motion. Activation energy is a phenomenological quantity used to describe the free energy barrier that an ion has to overcome for a successful jump between sites. Once displaced from the lattice, ions can diffuse and migrate between sites or interstitially. Table 2.1 list the sort of conductivities values.

Table 2.1. Conductivity, mobility and carrier concentration in electronic and ionic solids at room temperature [5].

Materials		Conductivity [$\Omega^{-1} \text{ m}^{-1}$]	Mobility, $\mu_{27^\circ\text{C}}$ [$\text{cm}^2 \text{ V}^{-1} \text{ s}^{-1}$]	Carrier concentration, $n_{27^\circ\text{C}}$ [cm^{-3}]
Electronic Conductors	Metals	$\sim 10^5$	$\sim 10^2$	$\sim 10^{22}$
	Semiconductors	$\sim 10^5$ - 10^0	$\sim 10^3$	$\sim 10^{10}$ - 10^{13}
Ionic Conductors	Superionic solids	$\sim 10^{-1}$ - 10^{-4}	$\leq 10^0$	$\leq 10^{22}$
	Normal-ionic solids	$\sim 10^{-5}$ - 10^{-10}		
	Poor-ionic solids	$< 10^{-10}$		

Superionic solids or solid electrolytes do actually cover different phases (crystalline and non-crystalline) of materials having in common a very high ionic conductivity (10^{-1} - 10^{-4} S m^{-1}). Solid electrolytes classification will be developed in the next sub-section. For the particular case of crystalline ionic solids, useful classification was proposed by Rice and Roth [27] based on the type of defect or disorder responsible for ionic conduction:

Type I: includes the ionic solids with low concentration of defects ($\sim 10^{18} \text{ cm}^{-3}$), which are usually poor ionic conductors at room temperature, such as NaCl or KCl. The main conduction mechanism is vacancy migration;

Type II: admits the ionic solids with high concentration of defects ($\sim 10^{20} \text{ cm}^{-3}$), which usually are good conductors at room temperature and possibly fast ion conductor at high

temperatures, namely ZrO_2 , CaF_2 , among others. Also in this type, the main conduction mechanism is vacancy migration;

Type III: best superionic solids belong to this class. They exhibit an ionic lattice similar to ionic liquids, composed by mobile ions, since they contain at least one type of atoms highly delocalized over the available sites. Crystalline solids exhibiting high ionic conductivity are termed superionic solids, fast ion conductors, solid electrolytes or hyperionic solids. The best-known examples are Na- β -Alumina and RbAg_4I_5 . The prevailing conduction mechanism is interstitial migration, and the moving ions actually can be described as forming pathways. Recently, conduction pathways in a solid electrolyte were directly observed [28] through the existence of nanometer-sized spots at the solid electrolyte/vacuum interface. These emission spots form a pattern and constitute the ending of bulk ion conduction pathways.

2.3. General classification of solid electrolytes

We have previously focused on conduction mechanisms for crystalline solid electrolytes and, in fact, the presented theory is fully valid only for those materials. However, solid state superionic conduction also exists in other phases and a general classification of these materials, according to Agrawal and Gupta [5], includes, besides crystalline electrolytes, some other types:

- amorphous-glassy solid electrolytes;
- polymer solid electrolytes;
- composite solid electrolytes.

Crystalline phase is the only where ions are ordered whereas the rest of the three different phases are not. Amorphous-glassy electrolytes and polymer electrolytes are microscopically disordered where composite electrolytes are macroscopically disordered materials.

As seen before, crystalline superionic solids can be understood as containing two sub-lattices: a rigid lattice within which a liquid like sub-lattice is enclosed and whose ions are movable. Ions are able to move interstitially or through vacancies, depending on the electrolyte.

In the case of amorphous-glassy electrolytes several attempts have been done to describe the ion transport mechanism in these atomically disordered materials. Several different models have been proposed and a brief summary and discussion of them can be found in the review produced by Agrawal and Gupta [5]. However, since the present project is based on crystalline electrolyte, theoretical aspects on other phases will not be presented. Amorphous solid electrolytes actually present some advantages over crystalline electrolytes, like isotropic ion conduction instead of preferential movement in pathways, absence of grain boundaries and easiness of deposition in thin-film form. However, generally amorphous electrolytes have ionic

conductivities lower than crystalline electrolyte's for the same movable ion and range of temperature.

Polymeric electrolytes are usually formed by the addition of ionic salts to complex polar polymers (extrinsic defects). In spite of frequently admitting the mobility of both positive and negative ions, as well as having advantageous properties such as flexibility, elasticity and transparency, polymeric electrolytes tend to have less mechanical strength, time stability and moderately high ionic conductivity (lower than $10^{-4} \Omega^{-1} \text{ cm}^{-1}$). Considering theoretical aspects, there are some phenomenological models to describe the ion transport mechanism but no fully accepted theory is available.

Finally, composite electrolytes are multiphase materials resulting on the mixture of different electrolytes in order to improve the total ionic conductivity. Therefore, crystal-crystal, crystal-glass or crystal-polymer composites might be produced and both phases simultaneously coexist in the composite system. One of the disadvantages of these compounds is their proneness to degrade upon ultraviolet radiation or heating. Once more, several models have been proposed and a summary might be found in the previously quoted review [5].

More recently a slightly different classification also based on the nature of the ionic conductivity was proposed by Karamov [29] which includes five groups:

- ionic crystals with low activation energy (usually less than 0.5 eV) and a large band gap. They can be said to be almost purely ionic (cationic or anionic) conductivity and electric insulators;
- non-stoichiometric compounds, whose elemental composition is not represented by a well-defined ratio, have both ionic and electronic conductivity;
- metals characterized by high solubility of hydrogen originating solid solutions with proton conductivity;
- non-stoichiometric compounds which become electrolytes when foreign ions are implanted;
- glasses with ionic conductivity.

Chapter 3. RbAg₄I₅ Solid Electrolyte

This chapter emphasizes the structural characteristics responsible for the high ionic conductivity of RbAg₄I₅. The influence of the different α , β and γ phases on ionic conductivity is qualitatively described, based on the modifications occurring in the crystalline structure. The nature of each different phase transition is also presented. Some recently used production methods are described.

3.1. Crystalline Structure and Ionic Mobility

RbAg₄I₅ is an example of a silver ion solid conductor where exceptionally mobile Ag⁺ ions are responsible for its high ionic conductivity (0.124 Ω^{-1} cm⁻¹ at 20°C [2]), presently the highest known. This electrolyte has very low electronic conductivity, 10⁻⁹ Ω^{-1} cm⁻¹ [30] and hence it can be considered an electric insulator.

This highly α conducting phase of RbAg₄I₅ is followed by two low temperature transitions, occurring at 209 K and 122 K [31] and leading to β and γ phases, respectively. The crystalline structure of RbAg₄I₅ can be generally understood as including a rigid component, composed of rubidium and iodine ions, and disordered silver ions, randomly distributed over a number of interstitial sites and therefore drifting relatively freely through the anion lattice [3]. However, different α , β and γ phases introduce slight modifications in the crystalline structure of RbAg₄I₅ which influence ionic mobility of silver ions and hence the ionic conductivity of the electrolyte itself.

In the high temperature α -phase, crystal structure belongs to space group P4₁32 [32] with lattice constant of 11.24 Å [33]. Each unit cell is cubic and contains four RbAg₄I₅: four Rb⁺ ions, sixteen Ag⁺ ions and twenty I ions. The twenty iodine ions form shared faces tetrahedron and the four rubidium ions are surrounded by highly distorted iodine octahedron, as represented in Figure 3.1 (a). Per each unit cell there are 56 sites available for solely 16 Ag⁺ ions thus promoting the formation of channels (pathways) where silver ions can move through, as shown in Figure 3.1(b). Ag⁺ ions in α -phase have very low activation energy, 0.11 eV [34], and therefore are virtually in a liquid state inside the rigid crystalline structure formed by I and Rb⁺ ions.

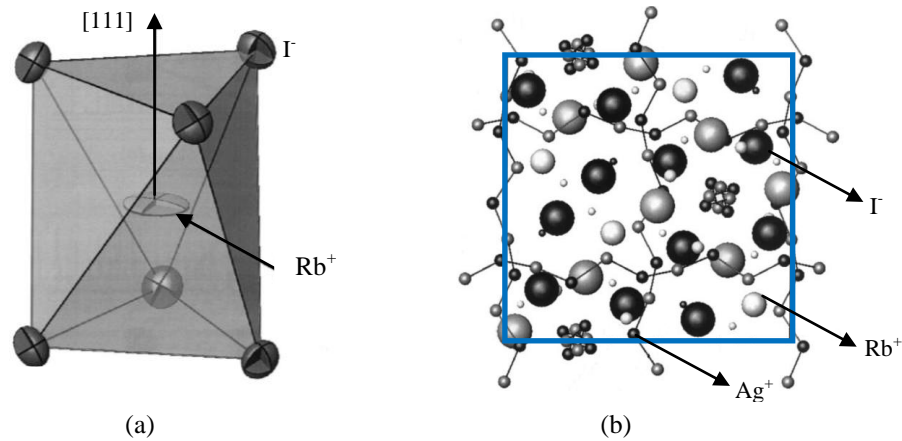


Figure 3. 1. Representation of the (a) distorted iodine octahedron around a Rb^+ ion and (b) crystal structure of RbAg_4I_5 , showing the cubic unit cell as the blue-lined box [33]. The larger spheres at right correspond to I, medium spheres to Rb^+ and small spheres to Ag^+ ions.

Considering 209 K transition, ionic conductivity initially seemed to vary very smoothly in the vicinity of the transition temperature, characteristic of a second-order transition. However, this transition was later proved to be first-order rather second-order by nuclear quadrupole resonance [35] and also by high-resolution thermal analysis on single crystal samples [36], which evidenced a small endothermic peak in the vicinities of 209 K. For this reason, sometimes this transition is also referred as "weakly first-order transition".

As the temperature decreases below 209 K, rhombohedral¹ β -phase (trigonal crystal system, rhombohedral unit cell) is formed. This belongs to space group $R\bar{3}2$ and presents a structure similar to α -phase [36, 37], as evidenced In Figure 3.2 (a) and (b). In β -phase short contacts only exist within but not between different Ag^+ clusters, showed in lower part of Figure 3.2 (b). However, in α -phase silver ions form a three-dimensional arrangement and short-cuts happened between 90% of the available sites [38], as represented in the lower part of Figure 3.2 (a). It seems that in β -phase silver ions move preferentially along the c -axis, establishing a preferential orientation for the movements of the ions and therefore the ionic conductivity is lower than in α -phase.

¹ The trigonal crystal system is one of the seven crystal systems, and the rhombohedral lattice system is one of the seven lattice systems. The trigonal crystal system includes crystals of both hexagonal and rhombohedral lattices. Therefore, some crystals might be in the trigonal crystal system but not in the rhombohedral lattice system. However, crystals in rhombohedral lattice systems always belong to trigonal crystal system.

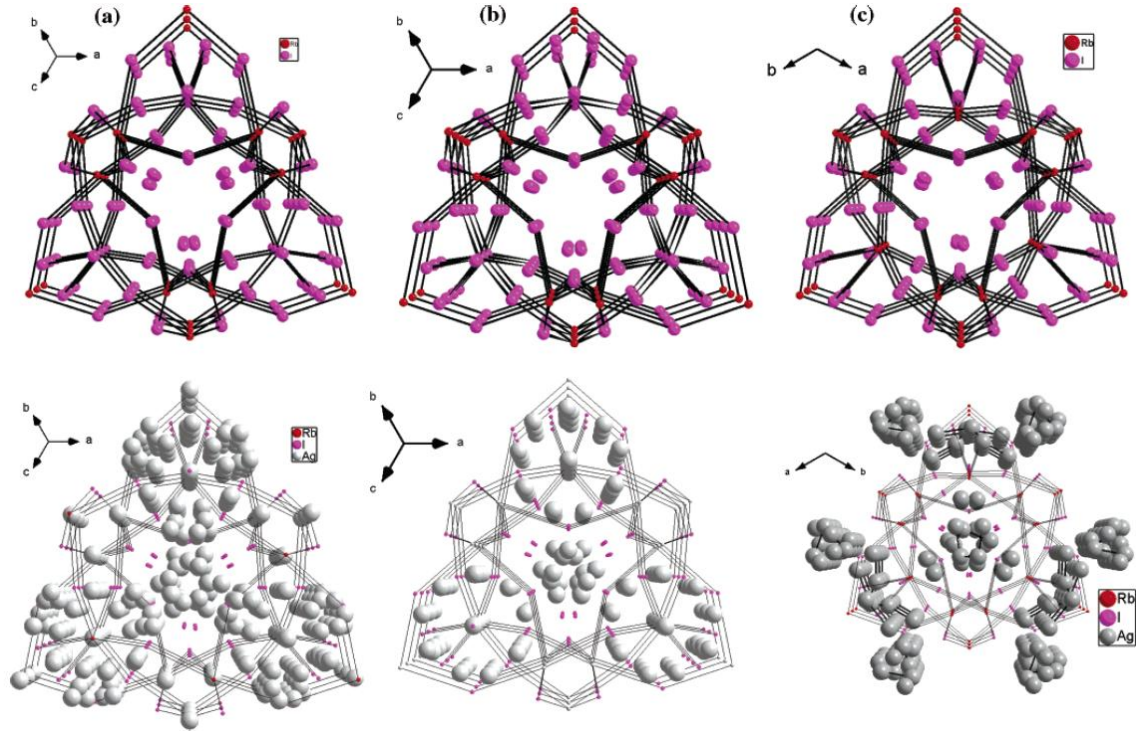


Figure 3. 2. Projection of the crystal structures of (a) α -RbAg₄I₅ at 295 K along the plane [111], (b) β -RbAg₄I₅ at 150 K along plane [001] and (c) γ -RbAg₄I₅ at 90 K along the plane [001]. The upper part presents the structures without silver ions and the lower part presents silver ions in a structure where Rb⁺ and I⁻ are downscaled [38].

Regarding 123 K transition, it causes a discontinuity of two orders of magnitude in ionic conductivity [4]. Below that temperature, trigonal γ -phase is obtained and belongs to spacial group P3₁21 [38]. In γ -phase fewer short contacts exist in contrast to the other two high temperature phases and several clusters are no longer interconnected, as can be observed in the lower part of Figure 3.2 (c).

Comparing Figure 3.2 (a), (b) and (c), one can see that the most pronounced structural changes occurring along α , β and γ -phases are related with the silver partial structure and the disorder of silver ions decreases with decreasing temperature. In summary, at low-temperature the movement of Ag⁺ ions tends to occur within isolated clusters instead of within a tri-dimensional sub-lattice liquid like lattice. The general dependence of ionic conductivity on temperature is represented in Figure 3.3. It can be seen that conductivity strongly increases with increasing temperature, showing Ag⁺ ions only move along lattice sites which are strongly dependent on crystal imperfections. However, there are also some evidences that, in the particular case of RbAg₄I₅ solid electrolyte, ionic conductivity might be nearly temperature-independent for temperatures below 75 K [40].

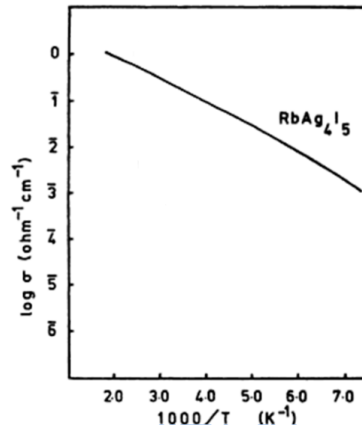


Figure 3. 3. Conductivity of Ag^+ in RbAg_4I_5 in the temperature range of 125 K and 1000 K [39] .

3.2. Synthesis, characterization and deposition processes

RbAg_4I_5 is produced using a stoichiometric mixture of RbI and AgI , whose phase diagram is represented in Figure 3.4.

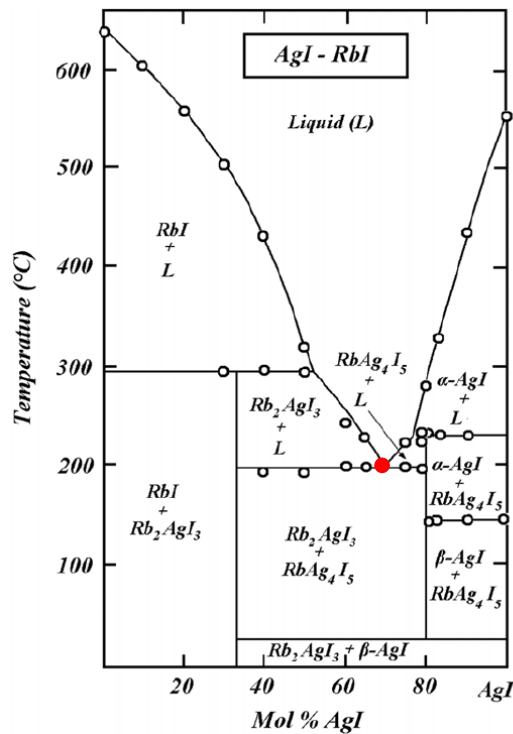


Figure 3. 4. Phase diagram of $\text{RbI}+\text{AgI}$ system [41]. The eutectic point (red colour) occurs at 197°C for a mixture with 30% of RbI .

The eutectic point occurs at 197°C , with a 30% of RbI . Two incongruent melting points can be found at 298°C for Rb_2AgI_3 and 228°C for RbAg_4I_5 . In particular RbAg_4I_5 is produced at that temperature if the mixture has 20% of RbI .

However, RbAg₄I₅ have been synthesised by several groups using slightly different stoichiometric mixtures of AgI and RbI.

Aiming to deposit RbAg₄I₅ through a thermal evaporation, Valov *et al.* [17] used a mixture of AgI and RbI in the proportion 78:22, which was melted at 400 °C for 2 hours in vacuum glass and then quenched and annealed at 160°C for 15 hours. The powder was directly used in the deposition through thermal evaporation. This process was carried out in vacuum using a substrate temperature of 70 °C and a deposition rate of 1 Å s⁻¹ in order to obtain homogeneous coverage and film crystallization.

The original proportion was kept by Shabanov *et al.* (20% of RbI, 80% of AgI) and the mixture was melted in an alundum crucible (fused alumina) in argon atmosphere. After cooling, the sample was kept at 200°C for 48 hours for homogenization [41]. In this case, deposition was not performed but α -phase electrolyte was successfully produced.

Yang *et al.* [42] also used 20% of RbI in the mixture and heated it to 400°C. According to the phase diagram in Figure 3.3, the mixture is liquid at that temperature and a slow cooling could result in a mixture of AgI, Rb₂AgI₃ and RbAg₄I₅. Hence, the mixture was rapidly quenched from 400°C to room temperature in order to obtain a pure RbAg₄I₅ phase. The mixture was then annealed at 150°C for several hours, to promote crystallinity and the stability of the electrolyte. In these experiments, pulsed laser deposition instead of thermal deposition was used to produce thin films.

Lee *et al.* [10] used a mixture of electrolytes with 17% of AgI, which was placed in a ceramic crucible and then heated to 450°C at a rate of 10 °C/min. After annealing for one hour at 450°C, the temperature was slowly decreased and the resulting sample was crushed into powder. In this case, samples for electrochemical nanopatterning were aimed. They were fabricated by placing the RbAg₄I₅ powder on silicon wafer and heating to 450°C at a rate of 10°C/min, resulting on crystalline electrolyte film with thickness below 1 mm.

Finally, an study on the percentage reactants was conducted by Cao *et al.* [43] determining that when the percentage of RbI in the range of 15-16 % of the initial mixture almost all single-phase films are formed during thermal evaporation. However, using the expected proportion of reactants, Rb₂Ag₄I₃ is also formed, showing a deviation from the expected composition, probably due to the partial decomposition of AgI during evaporation process.

There are other examples of procedures recently used to produce RbAg₄I₅ but this brief selection of procedures clearly evidences the absence of one straightforward routine to successfully produce the compound. Most likely each procedure was tried several times, with small adjusts in initial composition and experimental condition, such as temperature, before a successful result was obtained, i.e., an almost single phase crystalline RbAg₄I₅.

Even though the stoichiometric used the heating conditions of the mixture usually differ from group to group. Common procedures are the reduction of the bulk into powder and store it under vacuum conditions to prevent the degradation of the electrolyte. To verify the formation x-ray diffraction analysis is used and, less often, neutron diffraction analysis.

Chapter 4. Ion Source Based on RbAg_4I_5 Solid Electrolyte

This chapter describes the physical processes occurring at the surface of the electrolyte and at the silver/ RbAg_4I_5 interface. Under an accelerating voltage, Ag^+ ions migrate and diffuse through pathways in the electrolyte until reaching the apex of the micro-probe, where they are emitted. The system can be represented as an electrochemical system, with redox reactions taking place in it. The oxidation of silver atoms at the silver reservoir allows the entrance of new Ag^+ ions into the electrolyte. At the base of the Faraday Cup, incident ions are reduced into neutral species.

4.1. Brief description of the emitter system

The main components of the system are a silver tip, covered with RbAg_4I_5 film and an ion collector (Faraday cup), which grounded input electrode plays the role of an accelerator of the emitted ions. The silver tip covered with the electrolyte has a double purpose in the system: while the silver will constitute a reservoir of Ag^+ ions, the electrolyte is a mean for the movement and emission of those ions.

By applying a high potential to this assemble with respect to the grounded input electrode of ion collector, Ag^+ ions are emitted from RbAg_4I_5 and at the same time replaced by ionized silver atoms in the interface silver-electrolyte. Therefore, with this simple system ionic current can be measured.

Three main phenomena take place in the described ion emitter:

- compensation of emitted Ag^+ ions, through an oxidation reaction occurring at the silver reservoir/electrolyte interface;
- motion of ions inside the electrolyte under the presence of an electric field;
- emission of the Ag^+ ions from the electrolyte surface.

4.2. Oxidation and reduction of Silver Ions

4.2.1. An ions source as an electrochemical system

The usual components of an electrochemical system are two electrodes separated by an electrolyte, as represented in Figure 4.1 (a). In this type of systems, electrochemical reactions, also known as redox (reduction/oxidation), occur at the electrode/electrolyte interfaces.

In electrochemical reactions transference of electrons occurs between the electrolyte, where ions are the main charge carriers, and the metal or semiconductor, which have an enhanced capability to donate or remove electrons at the interface. As the redox term suggests,

an electrochemical reaction has two parts: reduction and oxidation. Oxidation corresponds to the lost of electrons from the reactant and reduction involves a gain of electrons of the reactant. The electrode where oxidation takes places is called anode while the electrode where reduction occurs is called cathode. It is important to stress that in electrochemical reactions, oxidation and reduction take place in distinct electrodes. On the contrary, in a chemical redox reaction oxidation and reduction occur at the same electrode. Besides, a chemical redox reaction is not limited to the interface region while an electrochemical reaction occurs exclusively at the interface between the electrode and the electrolyte.

Electrochemical reactions can hence be defined as chemical reactions depending on a potential difference in the interface, a region where electrical field is high enough to affect or induce a chemical reaction. When a voltage is applied between electrodes, a voltage drop occurs at the interface electrode/electrolyte, due to the accumulation of charges at the surface of the electrode, attracting opposite charges from the electrolyte, as represented in Figure 4.1 (a).

In our system, represented in Figure 4.1 (b), one of the electrodes is constituted by the silver reservoir covered by RbAg_4I_5 electrolyte. We considered only the very ending of the micro-probe, so that the sharpened shape is not visible. There is a vacuum volume separating this assemble from the collector electrode. When a positive voltage is applied, Ag^+ ions are attracted to the ion collector. The iodine negative ions are not likely to move in the opposite direction, since they belong to the rigid sub-lattice of RbAg_4I_5 , as Rb^+ ions. However, their attraction to the silver electrode in this situation is also symbolically represented in Figure 4.1 (b).

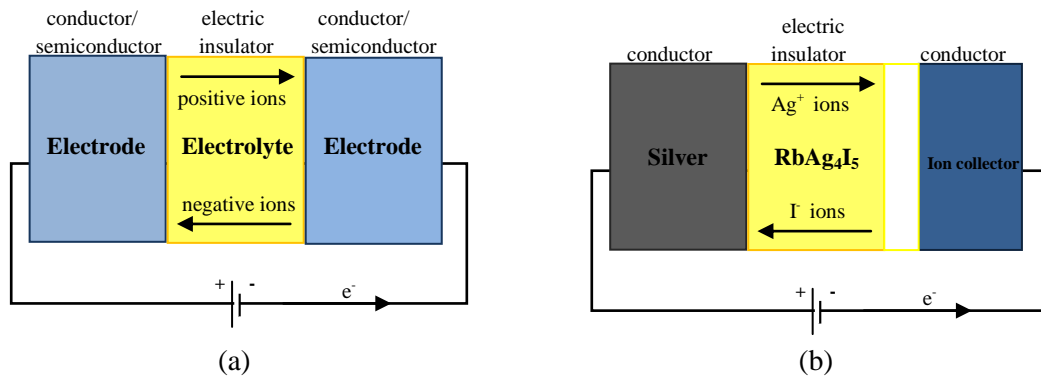


Figure 4. 1. Schematic representation of (a) a simple electrochemical system and (b) the proposed Ag^+ emitter system.

As a consequence of this movement of ions, the electroneutrality condition fails in the interface silver/electrolyte and a double layer of charges with opposite sign is formed: a positive layer in the metal side and a negative layer in the electrolyte side, forming the called double layer.

4.2.2. $\text{Ag}/\text{RbAg}_4\text{I}_5$ interface: double layer and pseudocapacitance

Several models have already been suggested to simulate the effect of the double layer in solid/aqueous interfaces namely by Helmholtz, Gouy-Chapman and Stern. The $\text{Ag}/\text{RbAg}_4\text{I}_5$ interface can also be realized as a solid/aqueous one, since in a electrolyte with high ionic mobility the motion of its movable ion is almost as free as in liquids.

Helmholtz model was the first proposed and the simplest one. In analogy with a solid state capacitor, two parallel layers of charges are separated at a fixed distance by solvent molecules originating a linear potential drop across the interface. In the Gouy-Chapman model the thickness of the double layer is no longer fixed but dependent on the electrical field (tending to maintain the order) and thermal effects (tending to make the arrangement random). Stern model, the most widely accepted, is a hybrid one, combining both previous models and considering some of the charges as being fixed and others as spread out. Figure 5.4 presents a general illustration of a double layer at the interface between a positive charged metal and an electrolyte in a solution whose solvent is water. As a consequence of the electrostatic forces between ions and the dipolar structure of the water, all ions in the aqueous solution are in their solvated form, having water molecules surrounding them.

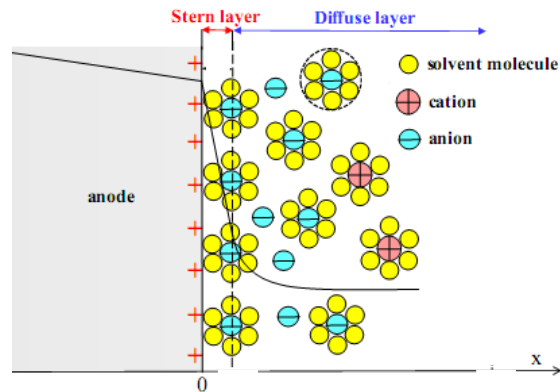


Figure 4. 2. Stern model of a general double layer formed in the interface between a positively charged surface and an electrolyte in aqueous solution [44]. Solvated cations migrate and adsorb to the electrolyte surface due to electrostatic forces. Potential drop is represented on the interface.

One consequence of the formation of a double layer is that the concentration at the bulk electrolyte is different from the concentration at the surface. In Figure 4.2 we can observe two distinct molecular layers. The Stern layer is defined as containing solvated anions strongly adsorbed to the anode surface. No single charges exist in this layer [44] but only beyond it, in a region where ions are mobile, the so-called diffusive layer. In this region, the influence of the electrolyte decreases and at a sufficiently large distance the concentration of species tends to the concentration of the bulk electrolyte.

This capacitive charging of the double layer allows to electrostatically store energy in proportion to the area of the double layers of the electrodes. It is important to notice that this process does not involve actually any electron transference but only physically adsorbed charges into the double layer. For this reason, the double layer capacitance is sometimes referred as purely electrostatic capacitance.

A different type of electrochemically storage, involving the passages of charges across the double layer, is also possible via the so-called pseudocapacitance. This phenomenon is also called Faradaic, attending to the electron transference between reactant species. From the experimental point of view it is difficult to distinguish whether charge is capacitively or Faradaically stored.

A thermodynamic measure of the stored energy is hence a combination of both chemical and electrical potentials, known as electrochemical potential. For certain species it is given by:

where μ is the chemical potential, z is the charge number of the species, F the Faraday constant and ϕ the electric potential in volts. The electrostatic potential corresponds to μ_{el} .

For an electrochemical system at constant pressure and temperature, another form to measure the energy is using Gibbs free energy. For a system presenting two electrodes, the change in Gibbs energy due to each half-cell redox reaction occurring at the respective electrode, is expressed by:

where ΔG corresponds to Gibbs free energy and ν to the stoichiometric coefficient of species i .

The polarity of ΔG is a measure of the tendency of a reaction to occur. Since in equation (4.1) electrodes were arbitrary defined as positive and negative, respectively, a negative value of ΔG means that the reaction in the positive direction (anodic) requires negative energy for being spontaneous. On the contrary, if ΔG is positive, it means that a minimum energy is required for the reaction in the negative direction (cathodic) to take place.

When a potential difference is externally set across the electrodes spontaneous reactions can be interrupted or non-spontaneous can be forced to occur, depending on the intensity and polarity of the applied potential difference. This potential is related to the Gibbs energy through the following equation:

where n is the number of electrons transferred in the reaction.

Considering our system, when a voltage difference is applied so that the silver reservoir is positively charged (anode) and the collector electrode is the cathode, silver atoms in the

reservoir are oxidized into Ag^+ ions at the interface $\text{Ag}/\text{RbAg}_4\text{I}_5$. The half-reactions correspond to:

According to the equations and and attending to the convention used, a more positive potential leads to more negative and thus tends to promote oxidation (i.e. loss of electrons) in the positive direction (anode). A negative potential (positive) tends to promote reduction (gain of electrons) in the cathode.

The suggested emitter system and the double layer with pseudocapacitance phenomena are illustrated in Figure 4. 3. In Figure 4.3 (a) ions do not experience yet the effect of the applied voltage and thus the net current of Ag^+ ions is zero. Fixed Rb^+ ions are not included but only movable Ag^+ ions and quasi-fixed I^- ions.

When high voltage is set between electrodes, silver atoms in the anode are oxidized into Ag^+ atoms, forming a double layer along with I^- ions in the electrolyte side, as represented in Figure 4.3 (b). If RbAg_4I_5 was usual electric insulator, recently originated Ag^+ would not be able to leave the positive monolayer. However, attending to the high ionic mobility of these ions in RbAg_4I_5 , Ag^+ ions at the interface can move into the bulk electrolyte and be emitted once reached the apex of the emitter. When ions are collected in a Faraday cup, neutralization takes place, through a reduction reaction.

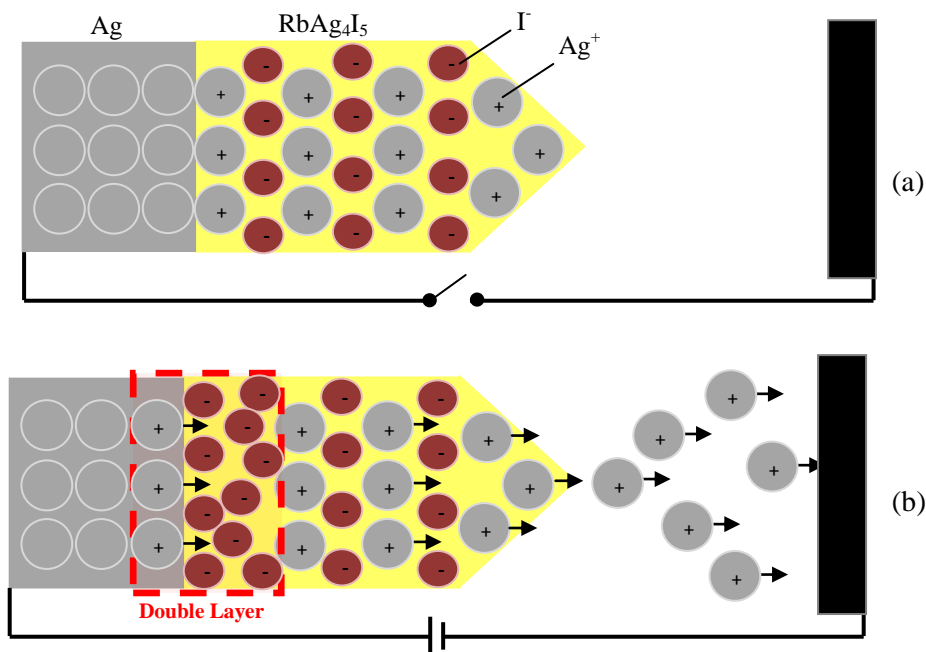


Figure 4. 3. Schematic representation of the emitter system (a) before high voltage is applied and (b) after the double layer is formed at the interface silver/electrolyte, where oxidation of silver atoms takes place.

4.3. Transport of Ag^+ ions under an applied voltage

Two main types of transport mechanisms can be considered in our electrochemical system - diffusion and migration. In systems containing aqueous electrolytes convection should be additionally regarded.

Under an electric field influence, ions move in a direction, which depends on the polarity of the applied field between electrodes. Cations migrate from the positively charged electrode towards the cathode, in the direction which is opposing to the electric field. Anions move in the direction of the electric field or from the negatively charged electrode towards the anode.

The flux density of ions migrating in these circumstances is expressed by the product between the concentration of species and their velocity:

where c is the concentration of species in mol m^{-3} , z the charge number of the species, u the mobility of the species in $\text{m}^2 \text{mol}^{-1} \text{J}^{-1}$, F the Faraday constant and ϕ the electric potential in volts.

Non-uniform concentration can result from the addition of extrinsic dopants or migration under an electric field. The existence of concentration gradient drives the species to move tending to make the concentration uniform. In that situation, the flux density is expressed by:

where D corresponds to the diffusion coefficient of species in $\text{m}^2 \text{s}^{-1}$. In the particular case of our proposed emitter system, the entrance of Ag^+ ions from the reservoir into the electrolyte crates a higher local concentration of those ions, which will tend to move across the bulk of the electrolyte. Another region with non-uniform concentration is probably the apex of the micro-probe, from where Ag^+ ions are emitted.

The net flux density can be approximated as a combination of the flux density associated to migration and diffusion:

4.4. Emission of Ag^+ ions

4.2.1. Field Ion Emission

In the focused ion beam developed by Escher *et al.* [19], whose structure is similar to our described in subchapter 4.1., Ag^+ ions are considered to be field emitted from $(\text{Ag})_{0.5}(\text{AgPO}_3)_{0.5}$ solid amorphous electrolyte.

Field ion emission is the extraction of a surface atom from its own lattice as an ion under the influence of very high local field. In general, field ion emission consists of two steps: the initial escape of atoms from the surface followed by ionisation when they move away from the surface [45]. Hence, the term *field emitted* as employed by Escher *et al.* [19] is not entirely accurate, since only escape without ionization occurs in case of solid electrolytes.

Also, field ion emission might refer either to field evaporation or field desorption [45]. In the first process, ions from a liquid or solid surface are repelled due to the magnetic field. In the second, adsorbed ions, which do not belong to the lattice, are emitted. From a theoretical point of view, there are no significant differences.

In the present work it is assumed that there is a negligible amount of foreign atoms in the electrolyte and hence we are dealing mainly with lattice ions. Admitting only the emission of lattice ions and considering it as involving one single process, namely escape, without ionization, the emission of ions from RbAg_4I_5 might be understood as a usual field evaporation escape process. This statement is also sustained by the existence of field evaporation from ionic liquids, usually by forming Taylor cones [46, 48], where ions are directly emitted from the electrolyte.

4.2.2. Field evaporation escape processes

Since the experimental evidence for conduction pathways in solid electrolytes was found [28], in the sequence of the development of ion source [19], it is possible to assume the end of those pathways at the surface of the electrolyte as the emission centres of ions. In our case, the sharpened shape of the emitter makes it possible to assume the apex as the main emitter centre, which is equivalent to admit that the pathways endings are mainly concentrated in that region.

In the general case of a solid electrolyte needle-shaped and set to a high voltage V , the electric field E generated at its apex is expressed by:

$$E = \frac{V}{r} \cdot f$$

where r represents the curvature radius of the apex and f is the *field reduction factor*, which introduces the necessary correcting electric field generated by a non-exactly-spherical shaped apex. Also, it is admitted that electric field does not change significantly within the micro-probe.

Once they reach the end of the pathways, Ag^+ ions are assumed to be emitted with zero kinetic energy and fly towards the neutral electrode. The final kinetic energy is proportional to the potential difference between electrodes and can be expressed by:

where q is the charge of ions. If the kinetic energy is aimed to be expressed in eV, W will be equivalent to $+I$ for Ag^+ ions.

Considering usual field evaporation escape processes, i.e. in the absence of pathways, atoms are emitted through electron or gas-atom bombardment or using thermally activated evaporation. This last can be used to estimate the influence of temperature in our system, if it is heated. According to the work developed by Forbes and Zurlev [49] the evaporation flux (atoms/s) is given by

where N is the amount of atoms at high risk of being field evaporated and ν is the field evaporation rate constant (s^{-1}) for these atoms. In the case of a micro-probe of RbAg_4I_5 the amount of ions at highest risk would be those in apex surface. More accurately, an estimate of the amount of pathways on that surface could be used instead of the entire apex area.

Field evaporation rate constant depends on the temperature following the Arrhenius type equation:

$$\nu = \nu_0 \exp\left(-\frac{E_a}{kT}\right) \exp\left(-\frac{eF}{E_0}\right)$$

and as usual ν_0 represents the pre-exponential factor, T the temperature of the emitter, k the Boltzmann constant and E_a depends on the electric field and is called field evaporation activation energy. An interesting parameter related with E_a is the so-called zero-Q evaporation field, meaning the electric field at which ν would become zero and hence ν_0 would have its maximum value.

Chapter 5. Production and Characterization Techniques and Equipment

The present chapter describes the basics of resistive thermal evaporation (RTE) technique, X-rays diffraction analysis (XRD) and time-of-flight secondary ion mass spectrometry (ToF-SIMS). RTE was used to produce RbAg_4I_5 films on silver tips and XRD to analyse the crystalline structure of the powdered electrolyte and micro-probes, before and after deposition. ToF-SIMS was used carrying out elemental characterization of the particles emitted by the micro-probes.

5.1. Resistive Thermal Evaporation

Resistive thermal evaporation belongs to the class of physical vapour deposition techniques, where films are formed by particles directly transported in gaseous phase from a source to the substrate. Thermal evaporation is based on the heating of solid materials to the sufficiently high temperature to reach its evaporation, followed by its condensation onto cooler substrate. This process is performed in a high vacuum chamber (- mbar) in order to control the composition of the deposited materials. There are several configurations based on the resistive heating of the target materials, which use an electric current passing through a foil, basket or crucible, where the materials are placed. A schematic view of resistive thermal evaporation system is represented in Figure 5.1.

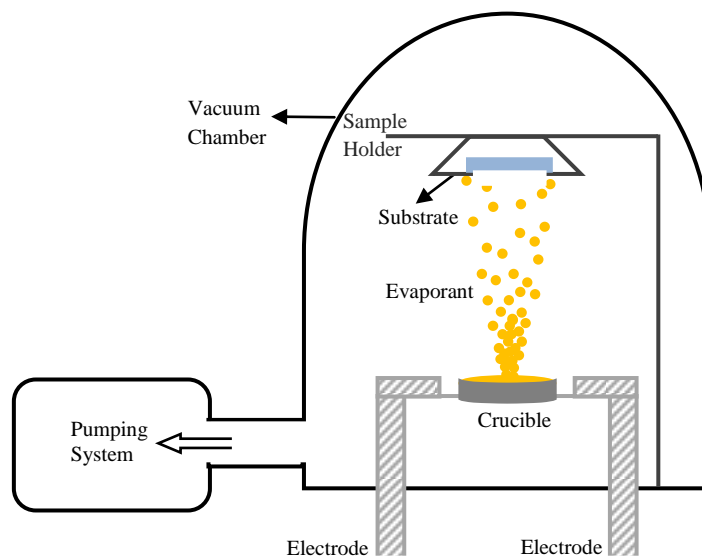


Figure 5. 1. Schematic view of resistive thermal evaporation chamber. Typically, a voltage in the range of 6-20V is applied to the electrodes and a current of 50-100A passes through the crucible.

The crucible, where the materials to be evaporated are placed, must be composed of chemical inert material with a high melting point like molybdenum, tungsten, tantalum, nickel or ceramics. The substrate can be mounted with a heater element or infrared lamp in order to reach a temperature that promotes crystalline film growth.

If the emitter source has a small surface area and the substrate is similar to a waffle, the relationship between the deposition rate (cm s^{-1}) at the substrate, v_d , and the evaporation rate from the source, v_e is expressed by:

$$v_d = v_e \frac{\cos^2 \phi}{r^2}$$

where θ and ϕ represent the emission and deposition angle respectively, ρ is the density of the evaporating material (g cm^{-3}) and r is the distance between source and substrate, as shown in Figure 5.2. With this type of source and substrate, the film thickness variation at the substrate can occur. If $r = 0$, the thickness at the centre of the substrate corresponds to $v_e \cos^2 \theta$ while at the edge it is $v_e \sin^2 \theta$. Usual solution is movable substrates, which rotate and translate simultaneously during deposition.

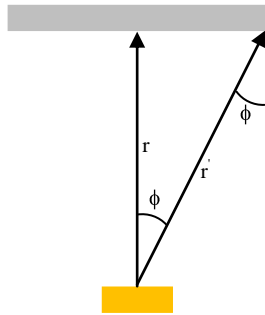


Figure 5. 2. Schematics representation of evaporation from a small area source.

Other disadvantages of this technique are poor adhesion and low film densities. In addition, in spite of RTE being used to deposit metallic films, such as aluminium, silver or gold, deposition of alloys is difficult to accomplish, attending to the different vapour pressures of the elements composing those materials. Evaporating this type of materials, the produced film will not have the same composition as the source, since the material with the lowest melting point tends to evaporate first (non-congruent evaporation). This problem might also occur with compounds with fixed composition, although some stoichiometric compounds might be stable at lower evaporation pressures.

In the framework of collaboration with CENIMAT, FCT-UNL, we used their thermal evaporation system (Figure 5.3) with a resistive heating molybdenum crucible to deposit RbAg_4I_5 powder on the silver reservoirs.

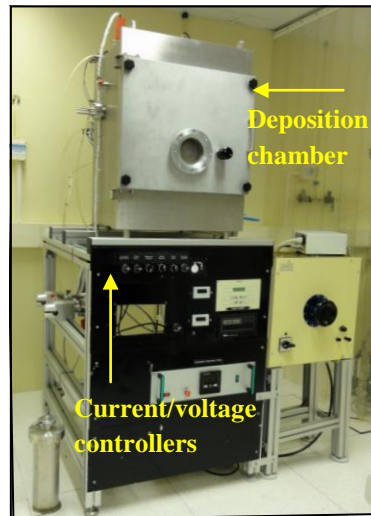


Figure 5. 3. Thermal resistive evaporation system at CENIMAT.

5.2. X-Ray Diffraction Analysis System

X-rays are electromagnetic radiation whose wave length is in a range from 0.1 to 10 Å.

X-ray diffraction analysis is a non-destructive technique used to characterize the crystalline structure of solid samples; it bases on the measurement of the angles and intensities of X-rays scattering from surface atoms. The experimental results are summarized in XRD spectra.

The conditions required for X-ray beam impinging a certain sample being elastically scattered can be understood using the Bragg's law:

where λ is the wavelength of the incident radiation, d_{hkl} represents the space between planes of atoms, hkl the Miller indices, used to identify different atom planes, and θ Bragg's angle. A simplistic model of the diffraction mechanism is represented in Figure 5.4.

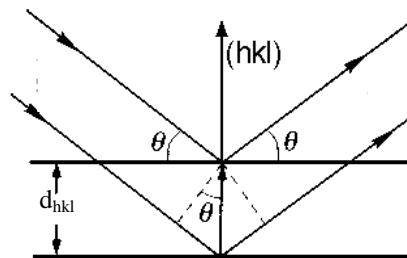


Figure 5. 4. Schematic presentation of X-ray diffraction. The plane $[hkl]$ is perpendicular to the plane of atoms.

Constructive interference of diffracted beams only occurs when Bragg's law is verified, admitting that atom planes spaced by d are parallels. This type of interference leads to the formation of diffraction peaks in the XRD spectra.

In the present project an automatic X-ray diffractometer *Philips Analytical PW 3050/60 X'Pert PRO* (Figure 5.5) was used, which includes a detector *X'Celerator* and the software *X'Pert Data Collector* for automatic data acquisition. The access to this equipment was possible due to the collaboration with the Department of Chemistry and Biochemistry, Universidade de Lisboa.

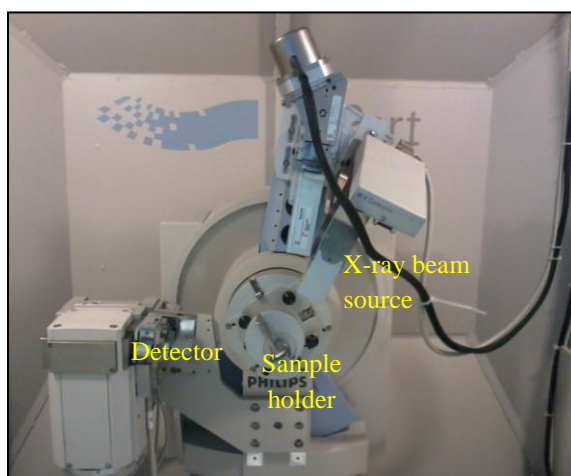


Figure 5. 5. *Philips Analytical PW 3050/60 X'Pert PR* diffractometer.

5.3. TOF-SIMS System

TOF-SIMS is surface analytical technique, which comprises primary ion beam sources with time-of-flight (TOF) mass analysis of the secondary ions.

Secondary Ion Mass Spectrometry (SIMS) is based on the emission of ionized particles ejected from a surface after energetic primary ions or neutrals impinge on it, which initiates a set of collisions between nearby adjacent atoms (collision cascade). Typically, the energy of primary particles is ranged from 0.5 to 30 kV. By energy transference during collision with surface atoms, a set of nearby adjacent atom collisions is initiated, as represented in Figure 5.6. Some of these collisions result on the emission of charged particles from the surface. Even though other secondary particles, like electrons, atoms, clusters or molecules might also be emitted, only charged particles (ions) can be analysed and detected by time-of-flight mass spectrometer.

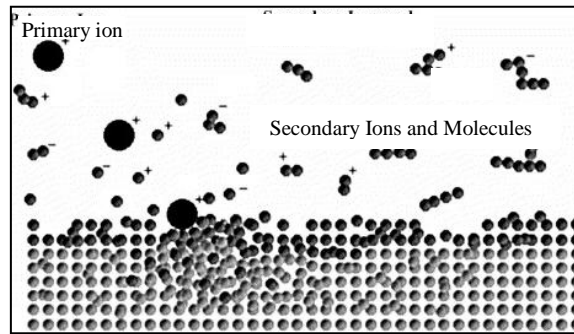


Figure 5. 6. Schematic representation of emission of secondary particles initiated by the impact of primary beam [50].

The basic SIMS equation for the secondary ion current of the detected species is expressed by:

where I_p is the primary current density (ions s^{-1}), Y the total sputtered yield (emitted ions/incident ions), P the ionization probability to charge state z , C the fractional concentration of species in the surface and T the instrumental transmission function. Due to the moderate dependence of T on m/z and the strong dependence between Y and m/z , I_z is not linearly proportional to C . This dependence is also referred as *matrix effect*.

Ion yield is defined as the fraction of sputtered atoms that become ionized, corresponding to SIMS ionization efficiency. Ion yields vary for the various elements, being influenced, for example, by ionization energy for positive ions and electron affinity for negative ions. Quantitative analysis of a sample can be performed using the relative sensitivity factor, according to the following equation:

$$I_z = I_p Y P C T$$

with S_z standing for the relative sensitivity factor for a certain element z and I_{ref} and C_{ref} being the secondary ion intensity for element z and reference element ref . The concentration of those elements in the sample, C_z and C_{ref} , can thus be determined with equation (5.1).

When the pulse of primary ions impinges the surface, pulses of secondary ions are accelerated to a given potential such that all ions have the same kinetic energy, eV , corresponding to

where V is the extraction potential.

Ions then reach a field-free region before the detector, with different velocities, v , depending on their mass m according to:

$$v = \sqrt{\frac{2eV}{m}}$$

and it can be demonstrated that the time-of-flight down a path length is given by

—

where L is the length of the free-field region. Lighter ions have higher velocities and hence reach the detector before heavier atoms. Therefore, attending to their masses, ions sequentially reach the detector. The ions with same masses are simultaneously detected.

It might happen that secondary ions with the same mass are not emitted with the same kinetic energy from the surface. In that case, energy distribution and time of flight of those ions both increase, thus decreasing resolution. To prevent this, time-of-flight analysers with energy compensation are often used. In this type of analysers, ions with higher energy travel along longer trajectories than others at lower energy, so that all ions with the same mass reach the detector simultaneously, independently of their initial energy.

Another problem that might occur during analysis is sample charging. Due to implantation of positive primary particles at the surface, the kinetic energy of emitted particles increases and can overcome the system detection limit. For charge compensation, a low energy electron beam impinging the surface is usual solution. To detect negative emitted particles, surface potential must be negative and high energy electron beam is used.

ToF-SIMS system can be operated in three different modes: static, dynamic and imaging. Static mode is used when the original surface should be affected as little as possible. Very low primary ion densities are used (less than 10^{13} ions cm^{-2}) making the detection of secondary ions from already bombarded surfaces almost negligible. The damaged area is less than 1% of the total surface area. On the contrary, in dynamic mode high primary ion density is used and large amounts of material are removed from the surface with a high erosion rate. A successive removal of top layers in the surface allows us to obtain spectra of the elemental depth distribution (depth profiling). By sweeping the primary ion beam over the surface, imaging mode enables the chemical mapping of the surface.

In the present project, an upgraded *VG Ionex IX23LS* ToF-SIMS [51] system was employed with a *Poschenrieder analyser* (Figure 18), which can be operated in static or dynamic mode and also as surface imaging. It includes two primary beam sources: gallium liquid metal ion-beam source and duoplasmatron. The first one is used in static and imaging modes and the second one in dynamic mode.

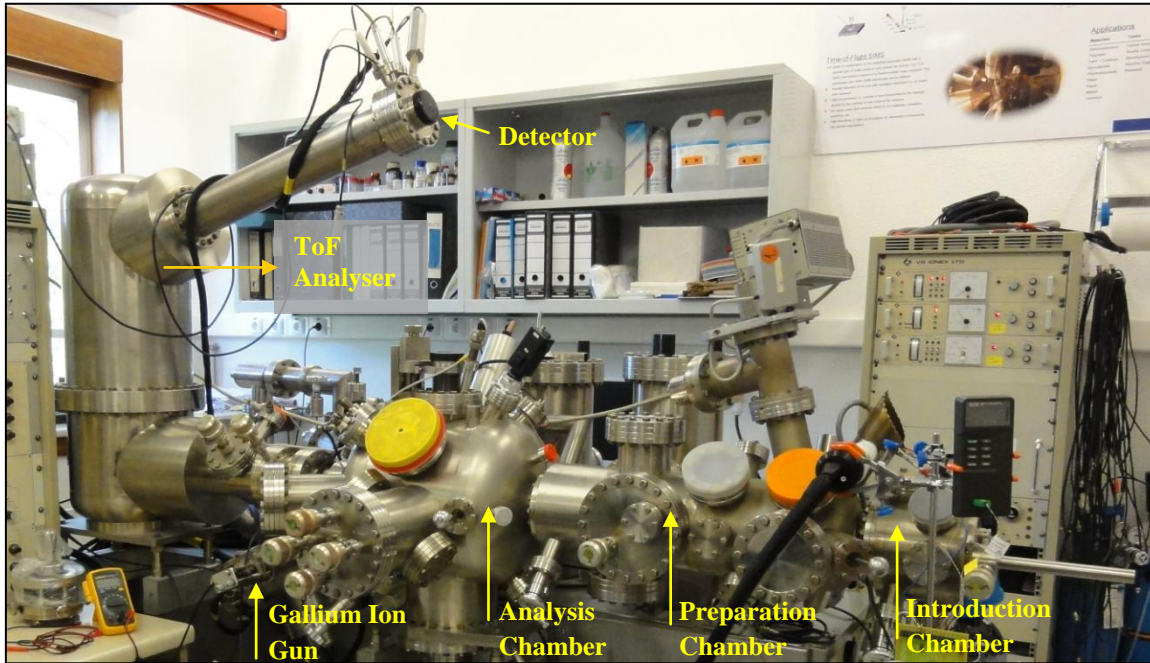


Figure 5. 7. ToF-SIMS equipment and its main components.

Chapter 6. Electrolyte and Micro-Probes Production

This chapter describes the production of RbAg_4I_5 from RbI and AgI initial materials and the results of XRD analysis of the compound produced. Also, the production of silver reservoir and its XRD analysis are referred. Finally, the deposition of RbAg_4I_5 on silver is described and the results of XRD analysis of the thin film are presented and discussed.

6.1. Electrolyte Production

RbAg_4I_5 was produced using RbI and AgI powdered electrolytes from *Sigma-Aldrich*. Attending to its simplicity, the procedure followed by Lee *et al.* [10] was chosen for preparing the final electrolyte. However, basing on the results obtained by Cao *et al.* [43], an amount of 16% of AgI was used, instead of 17% suggested by Lee *et al.* [10].

First of all, the composition of the reagents was confirmed by XRD analysis, to be sure that both electrolytes were properly preserved and no decomposition had occurred during its storage. After measuring and mixing RbI and AgI (84:16), the mixture was placed in a ceramic crucible. Then it was heated to 450°C at the rate of $10^\circ\text{C}/\text{min}$ in a programmable oven, followed by annealing for one hour at 450°C . After that, the compound was left to slowly cool inside the oven.

After cooling, a solid bulk of electrolyte was obtained with non-homogenous colour. The main part of the sample was light yellow, as expected for RbAg_4I_5 , however, besides this colour, orange and brown shades were visible in some regions of the electrolyte. Using a spatula, the bulk was carefully scratched and turned into three distinct yellow, orange and brown powders. Yellow powder was analysed with XRD and the resulting spectrum is presented in Figure 6.1. The procedure was entirely performed at the facilities of Department of Chemistry and Biochemistry, Universidade de Lisboa.

It was used a K_α X-ray incident beam, produced by a vacuum tube with copper anode, operated at 40 kV and originating an electron current flow of 30 mA. All diffractograms were obtained using 2θ continuous scan between 10 and 90° , a step size of 0.0170° and a scan step time of 50 seconds.

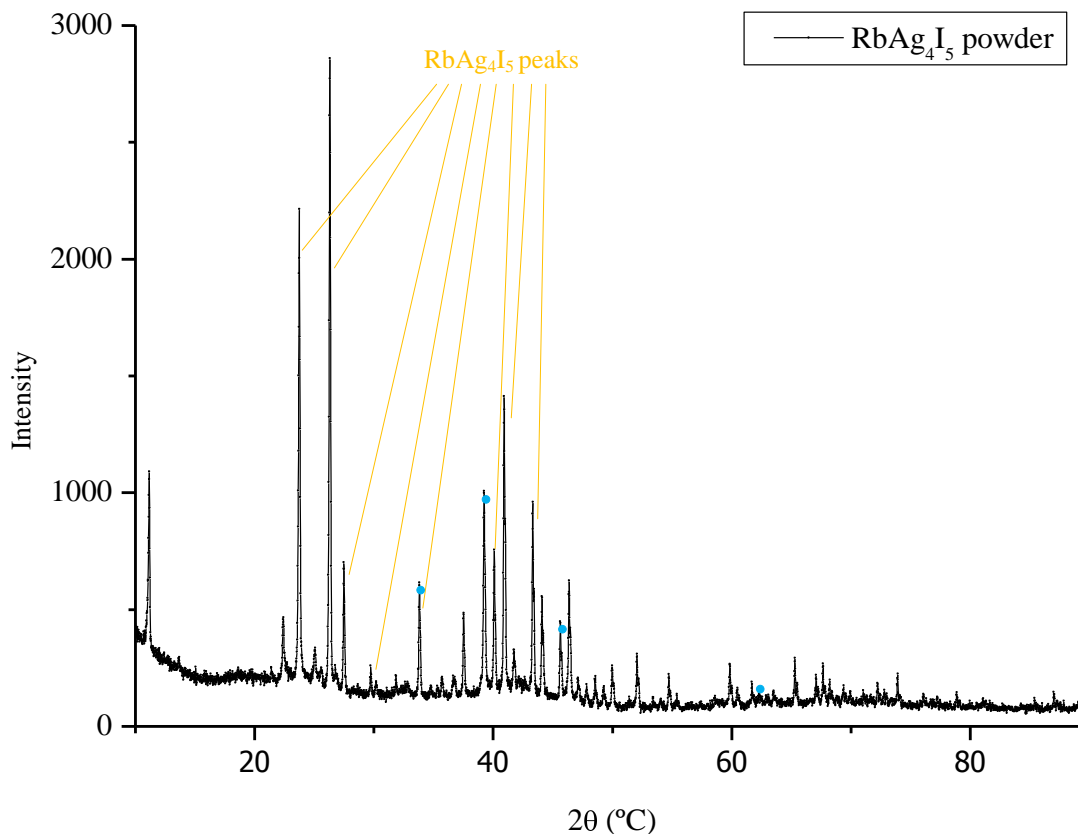


Figure 6. 1. XRD diffraction patterns of α -RbAg₄I₅ powder. The main peaks corresponding to RbAg₄I₅ are marked with lines and blue points represent peaks, which belong to α -AgI electrolyte.

The peaks expected for RbAg₄I₅ were searched in a powder diffraction manual, published by the *Joint Committee of Powder Diffraction Standards/The International Centre for Diffraction Data*, and the most intense of them were successfully identified on the diffractogram. Also, some peaks with lower intensity were identified as belonging to α -AgI. We can hence conclude that crystalline RbAg₄I₅ powder was successfully produced, although α -AgI electrolyte used as reagent has been only partially consumed. There are also several unidentified low-intensity peaks not likely to belong either to RbAg₄I₅ or α -AgI crystalline phases. Sometimes, a different compound might also be formed, for example, resulting on the reaction between a remanding reactant and the reaction product. However, it was not possible to index any of these compounds.

The present results can be considered as satisfactory for first approach, although totally pure compound was not obtained. In fact, the synthesis of crystalline compound is not straightforward process, frequently requiring adjustments in experimental conditions and several procedures repeating. Also, both synthesis and characterization of such materials are time-consuming procedures and a large amount of reactants might be used up until the required compound has been produced. Hence, in the present work, the following experimental activities were developed using the non-pure RbAg₄I₅ electrolyte.

6.2. Reservoir Production

A silver rod from *Sigma Aldrich* was melted and handcrafted in order to be shaped as represented in Figure 6.2; so, that it can be inserted in the micro-probe holder, connected to a DC high-voltage source.

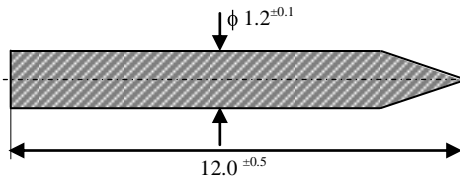
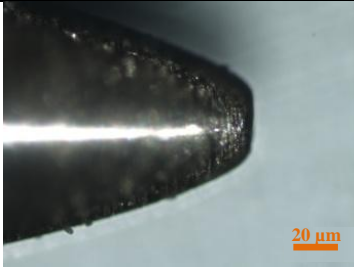





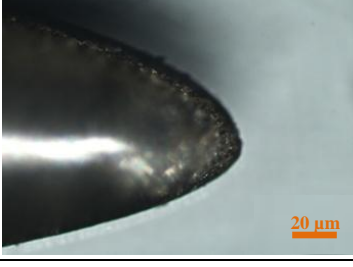



Figure 6. 2. Schematic drawing of the silver reservoir.

Four tips were produced and their extra polishing was later performed to obtain more sharpened apices and more smooth surfaces. As a result of their handcrafted production, the silver reservoirs present different apex diameters. Using optical microscope pictures, we estimated the diameter of each apex as well as the influence of the final polishing on the surface, as it can be seen in Table 6.1. After the ultimate polishing with sand paper, all tips produced have the radius of curvature lower than $5 \mu\text{m}$.

Table 6. 1. Images of the handcrafted silver reservoirs apexes before and after polishing with sand paper and their estimated diameters.

	Handcrafted tips	After sandpaper polishing	Apex diameter [μm]
1			4.4 ± 0.5
2			8.2 ± 0.5
3			6.1 ± 0.5
4			7.8 ± 0.5

The composition of reservoirs was studied using XRD technique. It was necessary, since in spite of initial high purity (99.999%) of silver rods, they were melted, shaped, sharpened and polished handcraft conditions. The correspondent diffractogram is shown in Figure 6.3, and the main silver peaks are indexed.

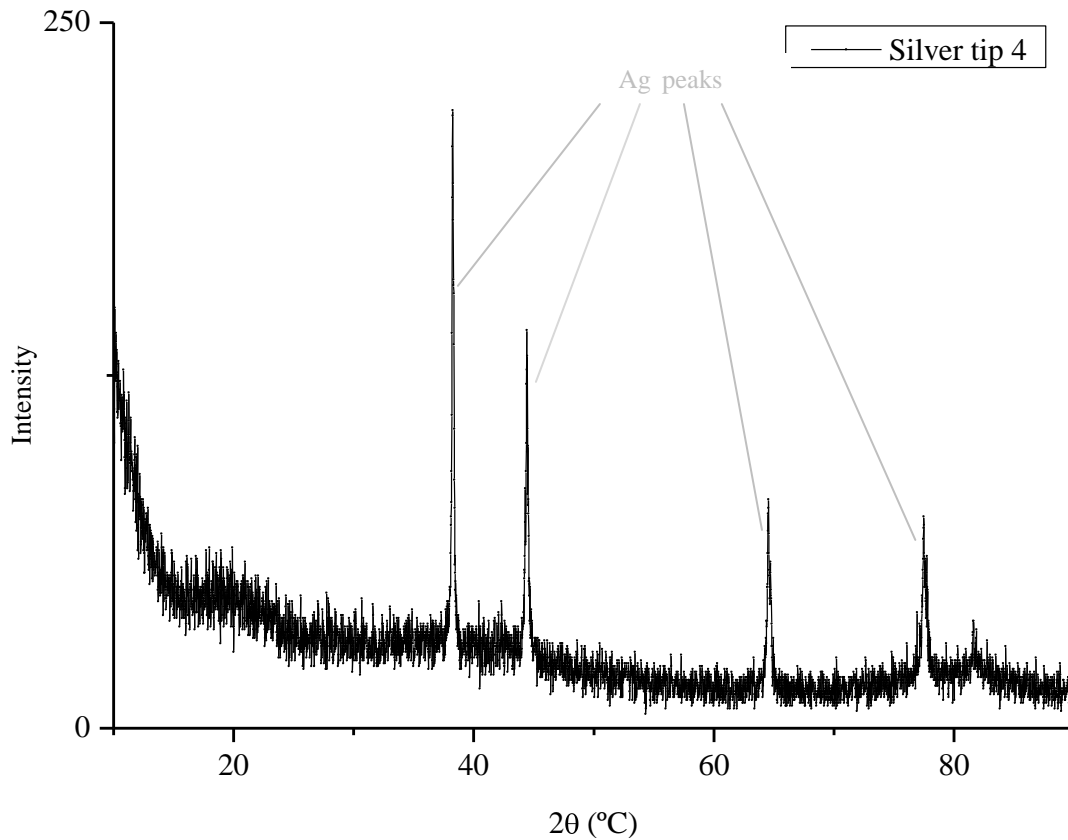


Figure 6. 3. XRD diffraction patterns of silver reservoir #4 ($7.8 \pm 0.5 \mu\text{m}$ of diameter). This tip was randomly selected for analysis and the composition of all other reservoirs was assumed to be similar.

6.3. Electrolyte deposition

RbAg_4I_5 powder was placed in a molybdenum boat crucible 22 cm below the substrate. This distance is similar to that used by Cao *et al.* [43] to perform the deposition. Tips were fixed to a sample holder using tape, made from kapton® polyimide film with silicone adhesive, which remains stable in a wide range of temperatures, namely from -269°C to 400°C . A view of the system before deposition can be seen in Figure 6.4. It is important to note that the vertical glass square could not be perfectly aligned with the crucible; as a result, the tip number 4 was the closest to the centre of the crucible.

After the pressure inside the chamber has reached 10^{-6} mbar, the electric current in the crucible was increase up to 100 A, and voltage was set to 0.6 V. The pressure increased to 10^{-4} mbar during evaporation and it was possible to observe the crucible becoming incandescent and the amount of electrolyte decreasing in it. Roughly five minutes and half later, the pressure decreased again to 10^{-6} mbar, meaning that the evaporation process was concluded. At that time, no electrolyte remained in the crucible.

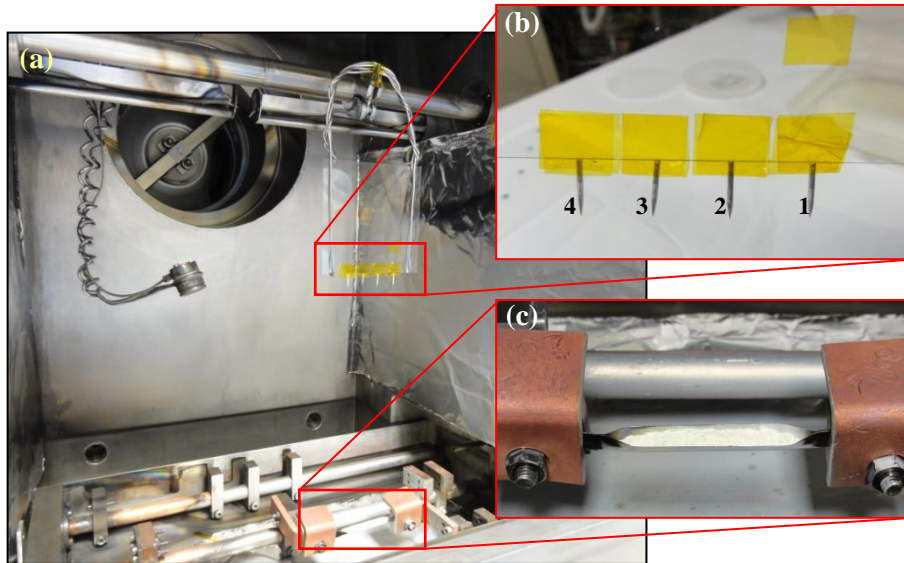


Figure 6. 4. Thermal evaporation chamber and details of (a) silver tips in the substrate holder and (b) RbAg_4I_5 powder electrolyte in the crucible before the deposition. From right to left, silver tips ordered from numbers 1 to 4, according to the classification used in Table 2.

After deposition, it was evident the presence of yellowish film on silver tips. Film thickness was measured on glass using a profilometer and estimated to be ca. 80 nm. The adhesion between film and glass was poor, making the measurement difficult. Also, the film thickness was not directly measured on tips to prevent their damage and contamination. Attending to their dimensions and sharpened shape, tips with deposited film can also be called micro-probes.

Micro-probe number 1 was selected for XRD analysis and the obtained diffractogram was very similar to that obtained for silver tips (Figure 6.3). This result can suggest that no film or very nonuniform film is deposited on this particular silver tip, which was the tip placed at the longest distance from the crucible. We do not discard the possible existence of a film whose thickness is actually lower than 80 nm, due to a lack of uniformity in the deposition, coexisting with areas without film. Also, attending to its distance to the crucible, micro-probe # 1 must be the one having the thinnest film, whose thickness is probably too low for XRD analysis.

Chapter 7. Experimental Set Up

This chapter briefly describes the experimental set up, including heating and vacuum systems, power sources and electrode assemblies. Faraday cup capacity to collect Ag^+ ion beam was tested using Simion® software and the main results of this simulation are also presented.

7.1. General overview

The experimental set up includes high voltage DC sources, electrometer, Pico Technology® data acquisition system (device and software), thermostat, thermometer and the emitter system itself. All these components are presented in Figure 7.1. The emitter system, placed in the preparation chamber of ToF-SIMS, comprises of two electrodes, one of which holds the micro-probe and is connected to a high-voltage source, and the other one performs the function of ion collector (Faraday Cup).

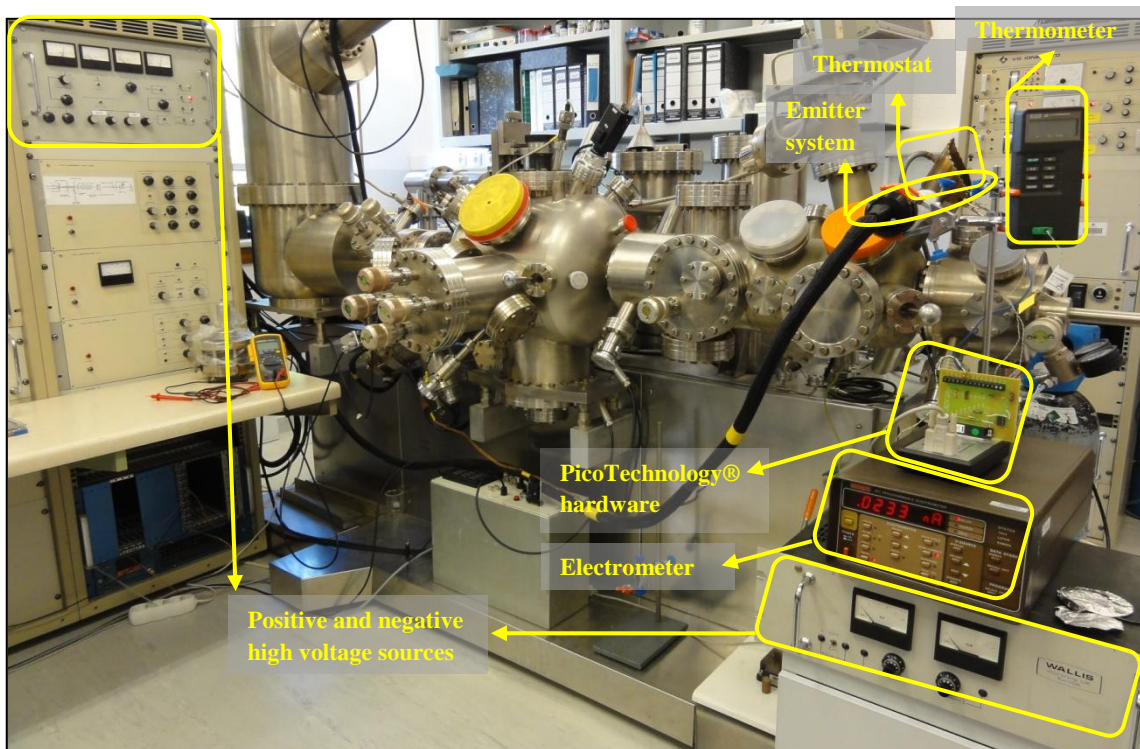


Figure 7. 1. Overview of the experimental set up. The emitter system is placed in the preparation chamber of ToF-SIMS at 10^{-8} - 10^{-9} mbar.

The components of the emitter system are shown in Figure 7.2 including both electrodes, as well as its connections to the rest of the experimental set up.

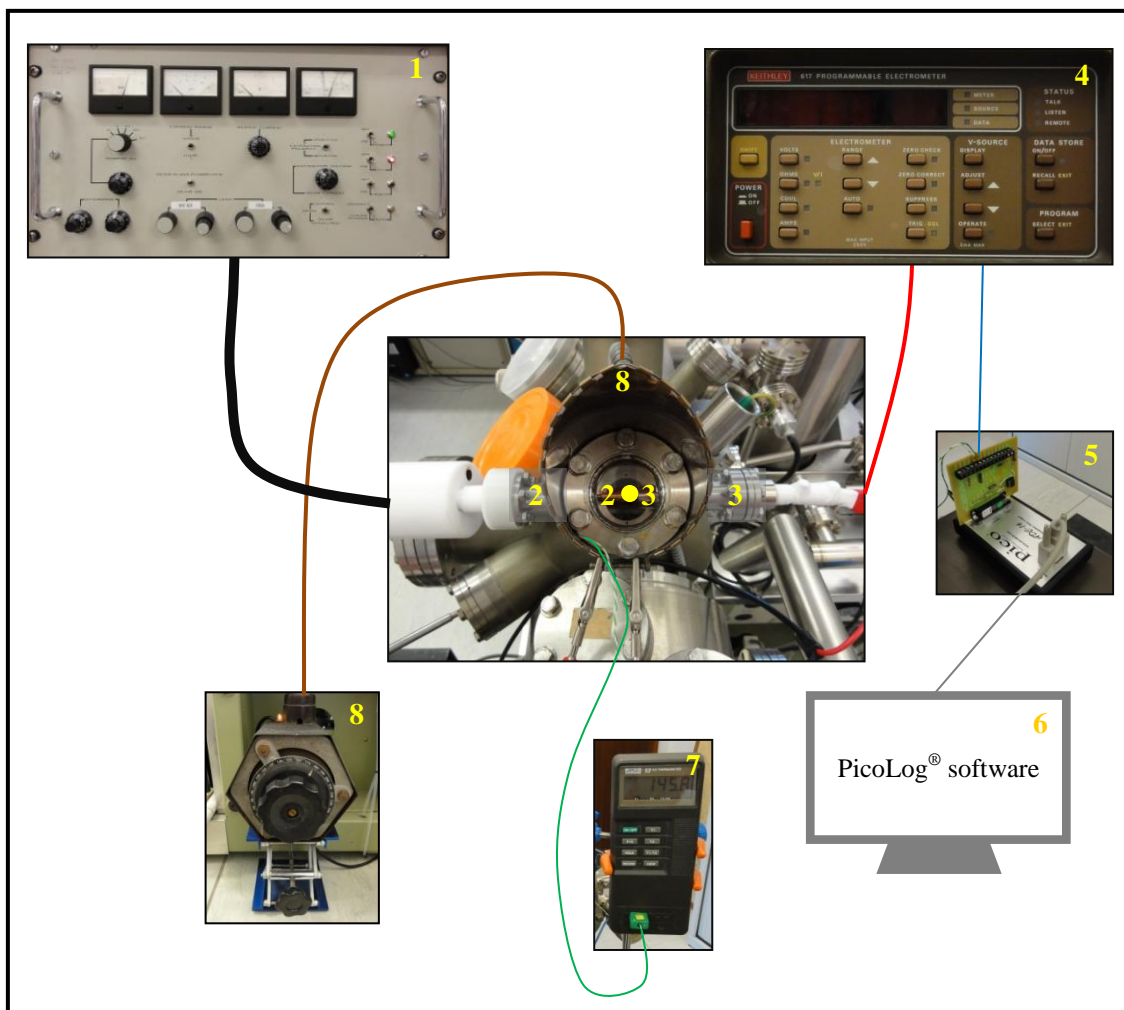


Figure 7.2. Emitter system (in the centre) and its connections. The small yellow dot is on the region between electrodes, travelled by the emitted particles. 1 - High voltage DC source; 2 - Electrode holding micro-probe; 3 - Faraday Cup; 4 - Electrometer; 5 - Pico Technology® acquisition data hardware; 6 - Computer/ PicoLog® software; 7 - Thermometer; 8 - Heating system. Ground connections are not shown.

7.2. High voltage DC sources

7.2.1. Material Description

A DC power source in the range of 0.5 - 22 kV is used to produce positive potential difference between the micro-probe and ion collector, which excites emission of positive ions from the emitter. To emit negative particles, a negative voltage in the range of 0.5 - 8 kV can be generated. We mounted insulation ceramics (Figure 7.3 (a)) around the high voltage connector and around the end of the high voltage cable itself (Figure 7.3 (b)).

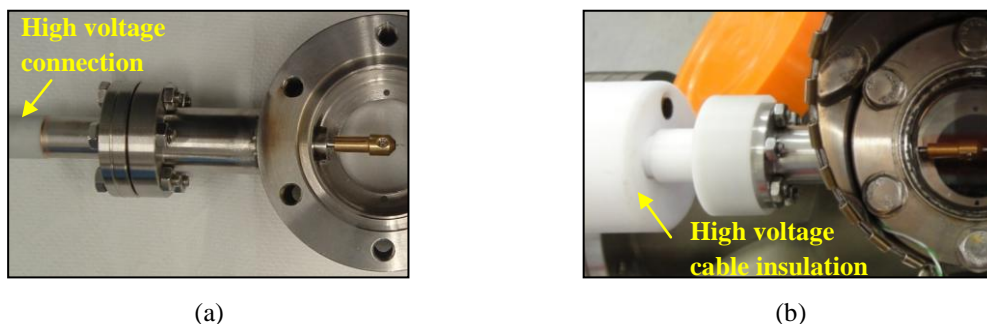


Figure 7.3. High voltage connection to the chamber: (a) without high voltage cable and before mounting the emitter system in the preparation chamber and (b) after that, with high voltage cable and insulation.

7.2.2. Faraday Cup and Electrometer

A Faraday cup is used to collect charged particles (positive or negative) in vacuum. The Faraday cup consists of three basic components: an electrically isolated stainless steel collector closed at the base, an external shield cup connected to the ground (both are visible in Figure 7.4 (a)) and a cap with an aperture, whose image is in Figure 7.4 (b).



Figure 7.4. Faraday Cup components: (a) inner and outer cylindrical electrodes and (b) cap. Ceramics was used to isolate the collector from the ground.

The Faraday cup is connected to a *Keithley 617 programmable electrometer*. This instrument displays the voltage drop across a shunt resistor and the correspondent electric current is indicated. When positive ions impinge the base of the cup, they are neutralized and the metal gains a small net charge. A Faraday cup can also work as an electron beam collector, directly producing an electric current.

To study the efficiency of the present Faraday cup as an Ag^+ ion collector, Simion® software was used. A micro-probe and the Faraday cup were reproduced in scale and the ionic emission was simulated for two different distances, 5 and 1 mm. The first corresponds to the maximum possible distance between the micro-probe and the edge of the collector, attending to the dimensions of the chamber where the system is placed. The second corresponds to a distance usually used in our experiments.

Cone direction distribution was used for the velocity of the emitted Ag^+ ions and 180° was set as the half angle of emission. The apex of the micro-probe was defined as having a radius of $33\ \mu\text{m}$, which is higher than the radius of our tips (less than $5\ \mu\text{m}$). The accelerating potential applied to the tip was $23\ \text{kV}$, also higher than the limit of our voltage source, and the ion collector was grounded.

The results of simulation are represented in Figures 4.4 and 4.5, for 5 and 1 mm respectively. In both cases, the trajectory of the ions was found to be very similar, with all ions reaching the base of the collector. The beam aperture barely changed with the distance, being higher when the distance is 5 mm, as expected. In conclusion, the projected system can collect approximately all emitted Ag^+ ions.

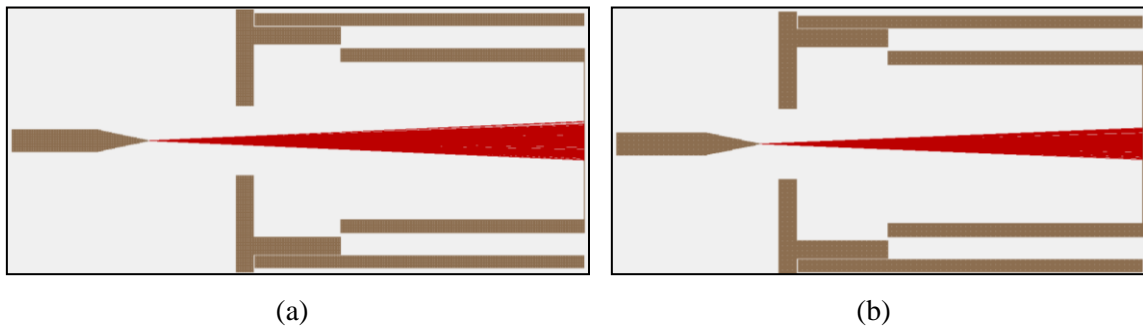


Figure 4.4. Simulation of Ag^+ trajectories using a distance of (a) 5 mm and (b) 1 mm between the micro-probe and collector. Resolution is $0.033(3)\ \text{mm}$ (i.e., 1mm corresponds to 30 points).

7. 2. 3. Pico Technology® acquisition system

The acquisition hardware in Figure 7.5 is composed of the *ADC-16 Data Logger*, connected to the computer and *ADC 16 Terminal Board* with 8-channels. One of the channels is connected to the analogic output of the electrometer through screw terminals. Their respective grounds are also connected to one another. By plugging straight into the channel, the voltage is directly measured and displayed in the *PicoLog* data acquisition software, where it is possible to measure, record and analyze the data.

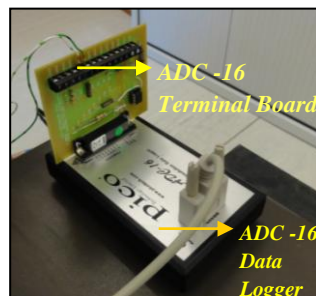


Figure 7. 5. Pico Technology® device for data acquisition.

7. 2. 4. Heating system and thermometer

A 250 V heater element with adjustable thermostat was used for heating the emitter system, through a brass piece around it. Increasing the voltage, the current will increase in the heating cable as well as Joule heating. The chamber walls in contact with the brass are heated by conduction and the micro-probe in vacuum mainly by radiation.

A thermometer is used to control the temperature of the walls around the emitter using a folding probe inserted between the brass and the walls.

7. 2. 5. Vacuum system

The emitter system is placed in the preparation chamber of the ToF-SIMS. This chamber is isolated from the introduction and analysis chambers by gate valves allowing us to replace the micro-probes without vacuum deterioration in the analysis chamber. This solution is cost effective, saving the efforts to mount and maintain an extra vacuum chamber, and uses an available high-vacuum volume.

The preparation chamber is pumped by a rotary pump *Alcatel 2004A*, through the samples introduction chamber, until primary vacuum is reached. High vacuum is obtained using a diffusion *Pump Edward EO4* with liquid nitrogen cold traps. The residual pressure in this chamber is usually in the range of 10^{-8} - 10^{-9} mbar.

Chapter 8. Experimental Results Analysis

In the present chapter, we summarize and discuss the experimental results. Included are the data on TOF-SIMS identification of emitted particles implanted into Ni foil and experimental dependencies of ion-beam current versus different parameters. These results demonstrate that the main components of the ion current are silver ions. Ion-beam current emitted from micro-probe #2 was analysed as function of time, temperature and accelerating potential.

8.1. Identification of the ion-beam content

In preliminary stage of our work, a set of micro-probes were produced by dipping a silver wire of 0.5 mm in diameter into melted RbAg_4I_5 electrolyte. By setting a high voltage difference between the micro-probe and the ion collector, the emission of positively charged particles was revealed through the measurement of a positive current in the pA range.

A representative ion current versus time of measurement graph obtained with the first set of micro-probes is showed in Figure 8.1. These data were collected at room temperature using a 20 kV difference between the emitter and ion collector.

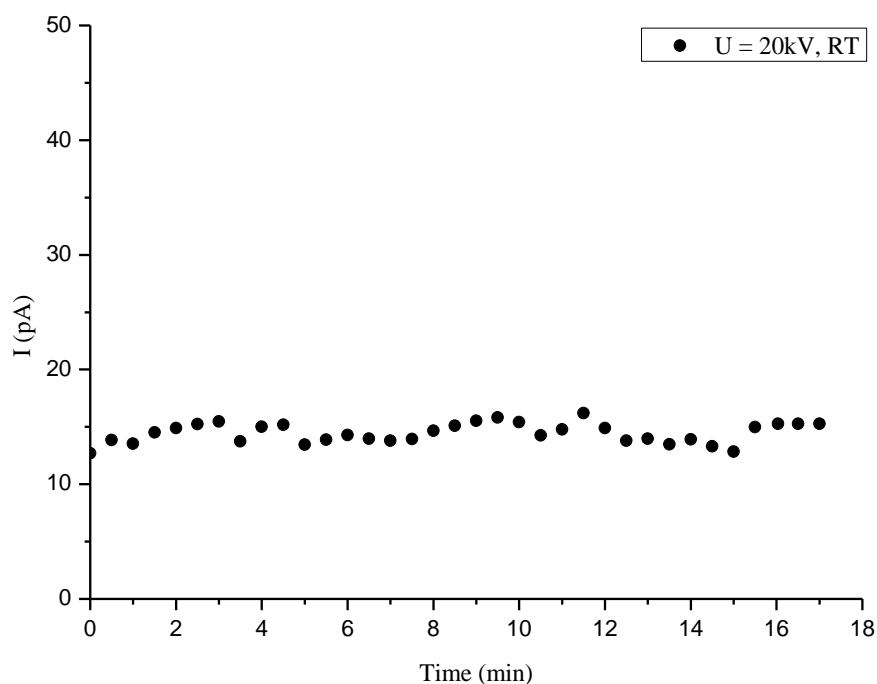


Figure 8. 1. Current-time graph for an emitter composed of silver wire dipped into the melted electrolyte (room temperature, 20 kV of accelerating potential).

The current was rather stable during the first minutes of emission and its average corresponds to 14 pA, approximately. In spite of being lower than the current obtained by Escher *et al.* [19], the current-time dependence exhibits a similar behaviour in terms of stability. Also, by replacing the solid electrolyte emitter for a pure silver wire of similar dimensions, we measured the ion current at level of the sensitivity of our pico-amperemeter (approximately null), which confirms the role of the electrolyte as the source of the emission.

In order to determine the composition of that ion beam, a circular nickel foil was analysed with ToF-SIMS technique before and after being exposed to the ion-beam at the Faraday cup base. In ToF-SIMS analysis a 15 keV Ga^+ ion beam was used, and the nickel foil was set to a voltage of + 5 kV. The results of the nickel foil analysis prior to ion beam exposure are presented in Figure 8.2.

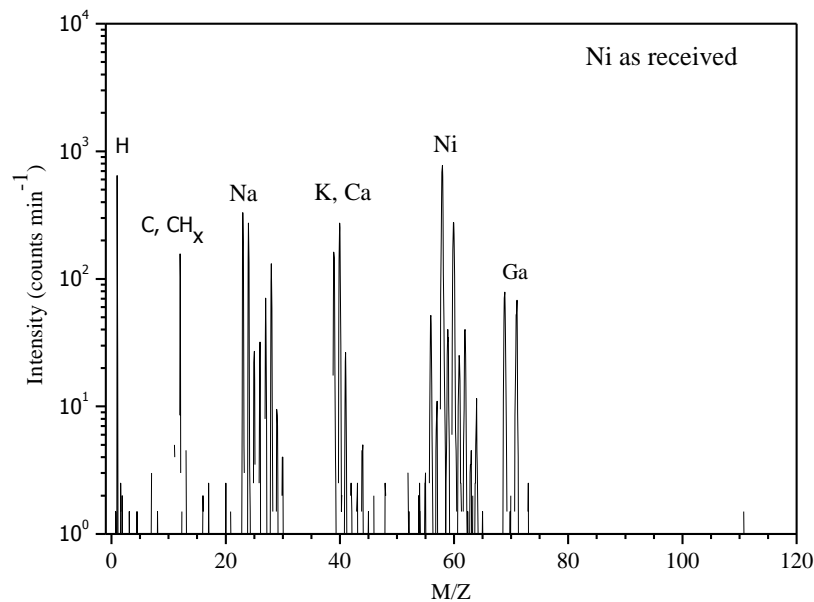


Figure 8. 2. Mass spectrum of positive secondary ions obtained for as-received nickel foil (before being placed inside the Faraday cup).

The spectrum clearly shows hydrogen, carbon and hydro-carbons, potassium, calcium, nickel and gallium ion peaks. Carbon is a common contaminant of vacuum systems; it is presented as hydrocarbons originating from lubricators, cutting oils, rotary vane pump oils, and residues of packing materials or fingerprints. Hydrogen is a component of the residual gas in vacuum chambers since it is more difficult than heavier gases to pump because of its high thermal velocity and its small molecular size. Potassium and calcium are surface contaminants with very high positive secondary ion yields. Gallium peaks correspond to the detection of sputtered Ga^+ primary ions implanted during analysis.

The nickel foil was then placed in the base of Faraday cup and high-voltage turned on. Emitted positive particles were collected during few hours. After measurements, the foil was removed and analysed once again with ToF-SIMS. The results are presented in Figure 8.3.

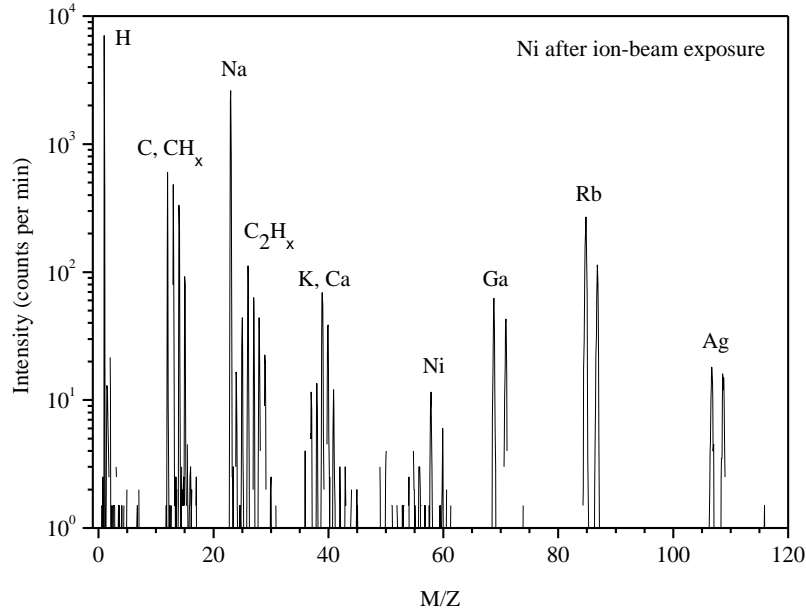


Figure 8.3. Mass spectrum obtained from a nickel foil after its exposure to the ion beam emitted from the electrolyte ion-beam source.

Four new peaks, which did not exist before, are now clearly observable in the mass spectrum, corresponding to the detection of rubidium and silver ions sputtered from the foil. The peaks corresponding to ^{85}Rb and ^{87}Rb isotopes attain a total 382.5 counts per minute. Silver isotopes peaks, ^{107}Ag and ^{109}Ag , have a total intensity of 32.5 counts per minute.

However, comparing the total intensity of those peaks is not enough to take any conclusion on the proportion between Ag and Rb content in the foil. In fact, Rb exhibits higher secondary ion yield in ToF-SIMS experiments, attending to their lower ionization energy (first ionization energy of rubidium and silver are 4,117 eV and 7,576 eV, respectively). Ionization energy is one of the factors influencing the secondary ion yield, which corresponds to the inverse of the RSF. These factors were found in the literature for silver and rubidium [52], and we used these data together with the experimental peaks intensities to estimate the actual content of Ag and Rb atoms in the foil (according to the equation (5.4)). The results of our estimation are presented in Table 8.1.

Table 8. 1. Experimental and corrected ratio of Ag and Rb secondary ion peaks in ToF-SIMS spectrum of the nickel foil.

$(\text{Rb}/\text{Ag})_{\text{RSF}}$ [52]	$(\text{Ag}/\text{Rb})_{\text{exp}}$	$(\text{Ag}/\text{Rb})_{\text{cor}}$
62.5	0.106	6.6

We can conclude that ca. 6.6 times more Ag species as against Rb were implanted into the nickel foil. With a great degree of probability, 6.6 is also the proportion between Ag and Rb in the emitted beam, since, according to the simulation in sub-chapter 7.3.2, all emitted particles are collected in the base of the Faraday Cup, where nickel foil was placed. Hence, we can affirm that a positive beam mainly composed of silver ions emitting of the electrolyte. Nevertheless, the exact charge of the emitted particles is unknown, although we expect Ag^+ ions as the main components of the ion beam. Also, it is not clear if Rb or Ag ions are emitted as clusters, or as atomic ions, since the mass-to-charge ratio (m/z) is not measured at this stage of work.

Finally, the main disadvantage of this set of micro-probes was very poor adhesion between the electrolyte and silver wire. During the experiments, it was found that the electrolyte tends to gradually crack and get separated from the silver, mainly due to the high malleability of the silver wire. The proposed solution was thermal deposition of the electrolyte on silver sharpened rods, whose production is described in Chapter 5.

8.2. Second set of micro-probes

The current dependencies on temperature, time and accelerating voltage were studied using all four produced micro-probes. Annealing was additionally performed as a way to increase and promote crystallisation of RbAg_4I_5 films on silver, since the XRD analysis on their crystalline structure did not give well-defined result. It was found that heating the micro-probes for 8 hours at 150°C actually improved the intensity of the ion current. The best results were obtained using micro-probe #2 (apex diameter of $8.2 \pm 0.5\text{ nm}$) and current dependence on temperature, time and voltage was studied for this probe. The results are presented and discussed in the next sub-chapters.

The fact that micro-probe #2 exhibits the best performance might be considered as an evidence of uneven electrolyte deposition on the silver tips. In fact, tip #1 apparently had no film and emitted no ion current, while micro-probes #3 and #4 demonstrated intermediate results in terms of current intensity. The difference in the micro-probes behaviour suggests that there are considerable differences in the quality and thickness of the films deposited. Also, it was not possible to establish a relation between ion-beam intensity and production conditions, namely, the distance from the silver tips to the crucible during evaporation. Micro-probe #4 and #1 were, respectively, the closest and farthest micro-probes to the crucible, but the highest stable current was obtained from micro-probe #2.

8.2.1. Current-temperature dependence

Using an accelerating voltage of 20 kV, the temperature was increased from room temperature to nearly 80 °C and its influence on the ion current is shown in Figure 8.4.

In the first region, up to 50°C, the current tends to remain constant. This is explained due to the difference between the heating mechanism of the metal surface, where thermocouple probe is attached, and the emitter micro-probe. The first is heated mainly by conduction and the second one only by radiation. Consequently, the temperature measured by thermometer differs from actual temperature of the emitter. Obviously, waiting for the stabilization of the current at constant temperature allows more accurate measurements but the heater takes several hours to stabilize at about a certain temperature. In fact, it is not actually possible to perfectly reach a constant temperature, since even at constant voltage there are small temperature increments over time inherent to the system auto-heating. In spite of that, very low heating rates and quasi-stable temperatures are possible to reach, compatible with current measurements.

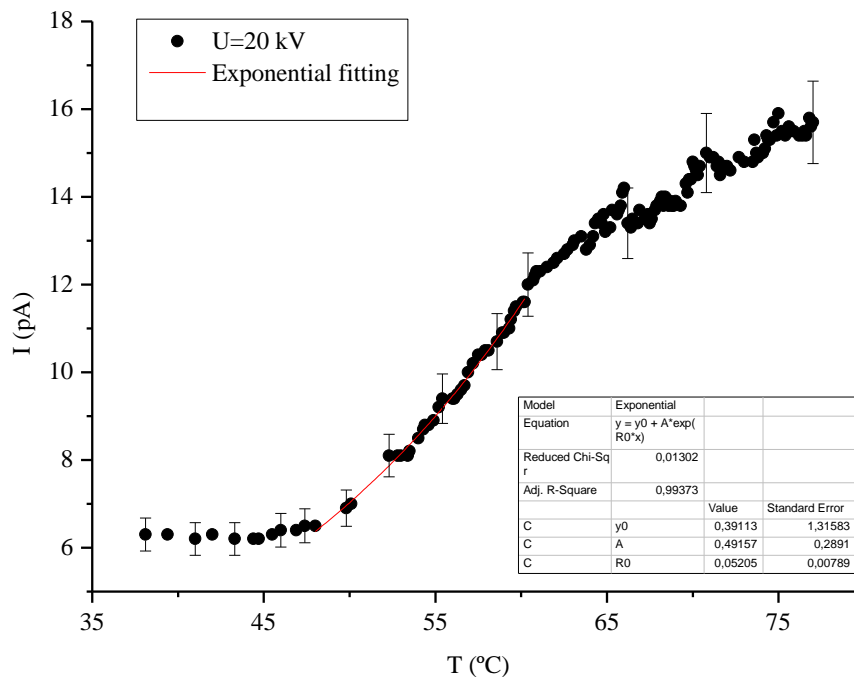


Figure 8. 3. Dependence of the ion current on temperature under an accelerating voltage of 20 kV.

The second main region, where current exponentially increases with temperature, represents the actual heating of the emitter.

The last region of the graph corresponds to readjustment of the heating rate, by decreasing the voltage of the heater system. Slight adjustments in voltage during heating process are necessary in order to reach the required temperature hence making a constant heating rate difficult to obtain.

The influence of temperature on the ion emission is not yet fully understood. Several of our experiments confirmed that this dependence has an exponential character. However, ionic conductivity, migration and diffusion of ions - all these processes depend on temperature according to Arrhenius type equation. Temperature contribution in ionic conductivity can be described using Arrhenius equation (2.18), promoting the production of holes and allowing ions to move in the electrolyte either through the holes or interstices. In the particular case of RbAg_4I_5 , the prevailing conduction mechanism is migration through pathways, channels formed by interstices between I^- and Rb^+ ions rigid lattice. Diffusion, moved by the existence of different concentrations of species in the electrolyte, also depends on temperature according to the same type of equation.

In spite of these Arrhenius type mechanisms, the emission current exponentially depends on temperature, at least in the range of temperatures below 150 °C. Hence, it seems that the escape process of the ions from the surface plays an important role on determining the current dependency versus temperature. Besides, field evaporation rate also depends on temperature according to Arrhenius type equation (4.10). Consequently, we can conclude that the nature of the escape process is significantly different from the field evaporation's.

Recent experiments conducted on ion thrusters based on an ion conductor emissive membrane report current dependency on temperature presenting an exponential-like behaviour [53]. However, the reported data does not present an exclusively exponential dependence over the entire range of temperature. Besides, it presents stabilization of the ionic current (oxygen ions) at higher temperatures, above 500°C. It is also necessary to take into account that the replenishing mechanism of negative oxygen ions by this membrane emitter differs from crystalline solid electrolyte emitter used in our experiments. Although the emission mechanism is the same, i.e. direct extraction of ions without ionization during escape, the replenishing mechanism is different, since a porous electrical-conductive layer is placed between the ionic conductor and the propellant (oxygen), to donate electrons for the oxygen atoms to become ions and then cross the ionic conductor.

8.2.2. Current-time dependence

After the temperature of the emitter has been stabilised around 92 °C and using an accelerating potential of 20 kV, the current was measured over a period of nearly one hour and half as presented in Figure 8.5. The average current value corresponds to 23 pA. In spite of the low intensity, the current is stable enough during the time of measurement. Similarly current stability was reported by Escher *et al.*[19], although the considered range of time is only 20 minutes.

The stability might be achieved due to the current saturation, which corresponds to the maximum intensity, which can be obtained at this temperature and voltage (nearly 23 pA). The

absence of significant emission peaks is an evidence of equilibrium between the replenishing rate at the interface Ag/electrolyte and the emission rate after instable emission during first minutes of acquisition even at constant temperature. In fact, both diffusion and migration processes are occurring simultaneously with migration due to applied field promoting differences in mobile ions concentration and hence their diffusion. The region of the apex is specially characterized by local differences in concentration, due to the permanent emission of ions. Finally, there is also the replenishing mechanism, strongly influenced by the potential at the interface, which depends on the charged species concentration in the electrolyte side. Consequently, the coexistence of all these mechanisms is likely to be the responsible for the initial emission instability.

Considering the lifetime of the emitter, the main limitation factor is the volume of the silver reservoir. Using a few grams of silver as reservoir replenishing, the emission current might be virtually infinite. However, we do not discard the possibility of depletion taking place at the interface silver/electrolyte, since silver atoms cannot move in the reservoir to compensate those oxidized into Ag^+ ions and moving into the electrolyte. If the depletion causes complete separation between the reservoir and the electrolyte, the emission current will decrease until no movable ions are left in the electrolyte.

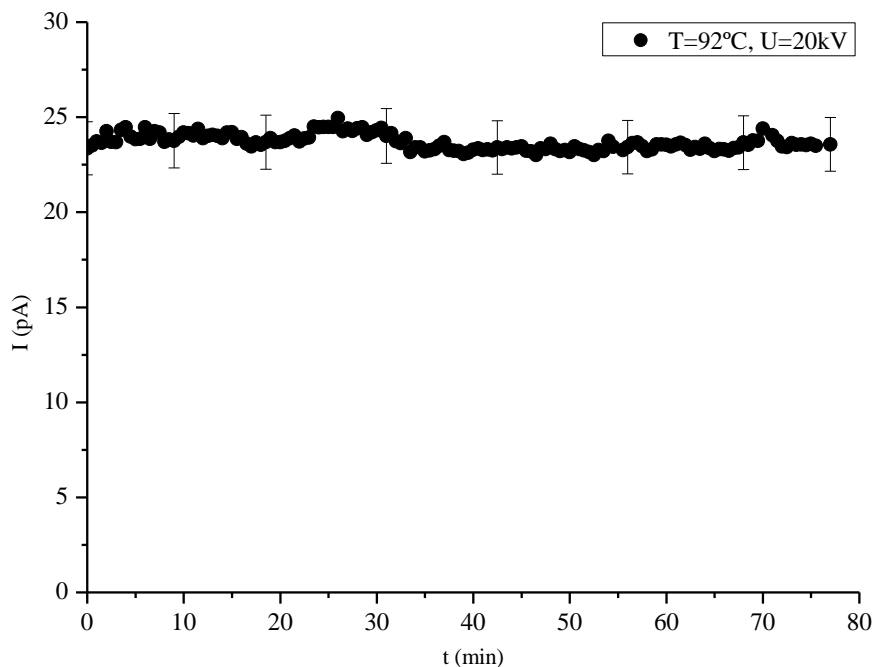


Figure 8. 4. Current-time dependence at 92°C obtained using an accelerating voltage of 20 kV.

By integrating the current-time graph we determined a stored charge of 1.8×10^8 F. Assuming that the apex has a spherical shape and considering half of its surface contributes to

the emission process, one can estimate the current density at the level of $20 \mu\text{A cm}^{-2}$. This is about of two orders of magnitude lower than the current density achieved by the thrusters with ion extraction from gas plasma. Some thruster regimes require a current density in the range of $1\text{-}10 \text{ mA cm}^{-2}$ [47] often obtained with liquid-metal field emission cathodes. However, there is also a room for microthrusters, which are useful to perform autonomous orbital maneuvering of tiny spacecraft.

Experiments conducted on ion thrusters based on ionic conductor emissive membrane demonstrate the ability to produce a current density near 0.3 mA cm^{-2} at 600°C but only $30 \mu\text{A cm}^{-2}$ at temperatures below 300°C [53].

8.2.3. Current-voltage dependence

At two different temperatures, around 77 and 92°C , the accelerating potential between electrodes was increased up to 22 kV , the emitted current was measured and the results are presented in Figure 8.6.

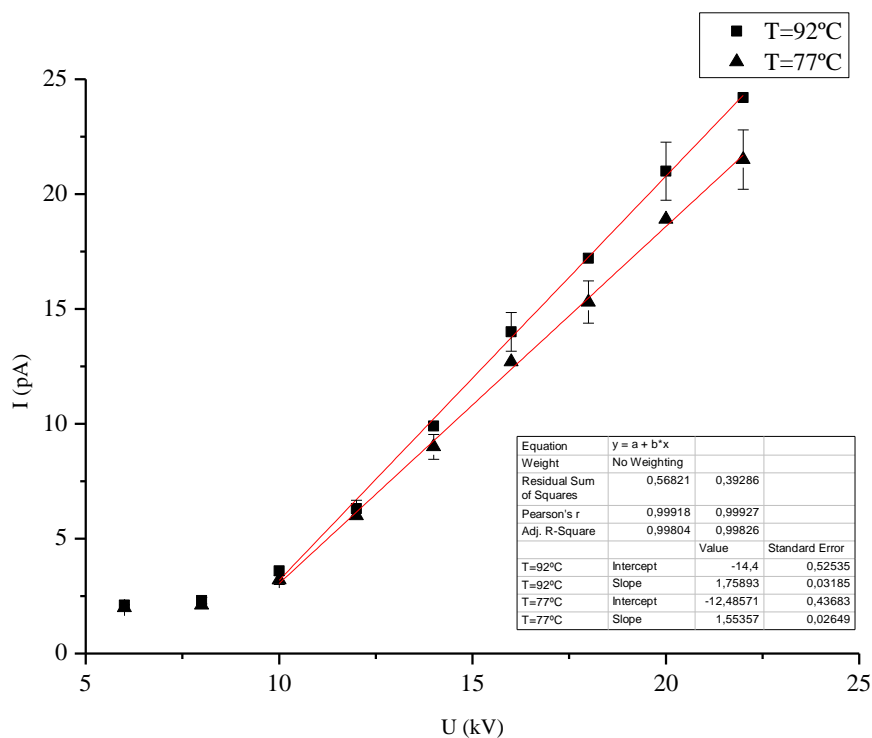


Figure 8. 5. Current-voltage dependence at 77°C and 92°C .

For voltages below 10 kV , ion current is at the same level as that in the absence of an applied field corresponding to the zero level current and to the absence of ionic emission. At the potential about 10 kV , ion emission starts, and the current value increases linearly with the

applied voltage demonstrating higher rate for 92°C as against 77°C. Similar dependence was obtained with a linear ionic liquid electrospray thruster [47]. At 20 kV the intensity of the electric field at the emitter apex is estimated to be ca. 44 kV cm⁻¹.

Chapter 9. Conclusions

In this thesis, an ion emitter based on RbAg_4I_5 was developed and studied. All the emitted particles can be considered as reaching the ion collector and effectively contributing to the measured current. It was shown that silver ions (atomic or cluster) make a major contribution to the measured ion current, although rubidium ions with concentration of 6.6 times lower than silver were also detected in the ion beam. Since Rb^+ ions could not move away the electrolyte, the emission of clusters composed of silver and rubidium ions is one of possible explanations of this phenomenon.

Ion current was measured as a function of temperature, time and accelerating voltage. Temperature has exponential influence on the current increasing. Some difficulties exist on keeping the heating rate constant. A current in the level of 23 pA, at 92°C and 20kV of extraction voltage, was proved to be stable for almost ninety minutes and a long life can be supposed for the emitter system. There is also a room for the improvement since current tends increase with temperature and accelerating voltage.

From the theoretical point of view, there are no consistent models to fully predict or explain the behaviour of ion emission directly from a solid electrolyte under an applied electric field. In this thesis, a simple model using field ion emission concepts is discussed. The oxidation process occurring at the interface $\text{Ag/RbAg}_4\text{I}_5$ was explained by considering the emitter system as an electrochemical device.

We also noticed that electrolyte production and deposition are crucial and rather challenging/complex processes. Considering the synthesis, several recipes with different complexities are available in the literature. However, the absence of one straightforward process indicates that obtaining a crystalline structure is demanding process, likely to require several attempts and adjustments. In addition, the synthesis should be controllable by XRD since the crystalline structure of the compound must be validated. In this thesis, a very simple procedure was chosen to produce RbAg_4I_5 and its structure was found to be crystalline. However, the produced electrolyte is not pure since traces of AgI initial compound were also found.

The thermal evaporation and deposition are even more challenging processes. If the temperature of the substrate is not high enough, the electrolyte might be deposited as a non-crystalline compound. Experimentally, we obtained non-uniform deposition on silver tips. It is not clear if the deposited electrolyte thin film was amorphous or if there was a lack of film in the region analysed by XRD. Also, the deposition on small area substrates like silver tips involves a considerable waste of evaporant electrolyte. Several adjustments in the deposition

chamber and procedure are necessary for optimizing and making the process cost effective. For instance, it is crucial to set and control the crucible and substrate temperature. Also, the ideal crucible-substrate distance must be adjusted as well as the adhesion electrolyte-silver tips.

Some improvements should be done in the experimental condition and set up.

Direct mass-spectrometric measurements of the emitted particles should be performed to determine their mass-to-charge ratio. Although the main contribution of Ag^+ ions is expected, cluster and molecule ions might be emitted too. The study of the emitted particles also contributes for the understanding of the emission process.

The present heating system does not allow controlling an actual the micro-probe temperature (its dependence on time) and requires several voltage adjustments during heating, changing its rate. Although expensive, and external infrared heater directly pointed in the direction of the ion emitting electrode could be a possible solution for obtain accurate stable temperatures.

In further works, would be interesting to study the running time of the emitter using reservoirs with different volume and micro-probes with electrolytes deposited on non-silver reservoir. It will be interesting to study the influence of the apex diameter on the ion emission since in present work the deposition of electrolyte on different silver tips was not uniform. However, in spite of some problems and troubles above discussed, the main task of our work has been fulfilled. We have demonstrated that crystalline solid electrolyte can be used as a source of ions. The developed ion-beam source has produced a stable current over a long period with minimal expenditure of energy and reservoir's material. Its design is simple and manufacturable. We expected that such sources would have potential applications in materials science and spacecraft engineering as principal elements of miniaturized electric propulsion systems (ionic thrusters).

References

- [1] Y. F. Y. Yao, J.T. Kummer, Ion exchange properties of and rates of ionic diffusion on beta-alumina, *Journal of Inorganic and Nuclear Chemistry*. (1967), 2453-2466.
- [2] P. D. Greene J.N. Bradley, Solids with High Ionic Conductivity in Group 1 Halide Systems, *Trans. Faraday Society*. (1967), 424–430.
- [3] J. N. Bradley, and P. D. Green, Relationship of structure and ionic mobility in solid MAg_4I_5 , *Trans. Science*. (1967), 2516-2521.
- [4] B.B. Owens, G.R. Argue, High Conductivity Solid Electrolytes: MAg_4I_5 . *Science* (1967), 308-310.
- [5] R. C. Agrawal, R. K. Gupta, Review Superionic solids: composite electrolyte phase – an overview. *Journal of Materials Science* (1999), 1131–1162.
- [6] M. De Rossi G., Pistoia, A. Scrosati, Reversible Solid-State Battery with RbAg_4I_5 as Electrolyte, *Journal of The Electrochemical Society*. (1969), 1642-1646.
- [7] B.B. Owens, B.K. Patel, P. Skarstad, Performance of $\text{Ag/RbAg}_4\text{I}_5/\text{I}_2$ solid electrolyte batteries after ten years of storage. *Solid State Ionics*, (1983), 1241-1245.
- [8] B.B. Owens, Twenty years storage test of $\text{Ag/RbAg}_4\text{I}_5/\text{I}_2$ solid state batteries. *Solid State Ionic*, (1993), 243–249.
- [9] G. Taralunga, C. S. Bolla, E. M. Rus, D. M. Constantin, Batteries with RbAg_4I_5 for pacemaker. *Romanian Journal of Biophysics*, (2004), 37–41.
- [10] R. M. Lee, F. B. O’Hayre, T. Prinz, M. , Electrochemical nanopatterning of Ag on solid-state ionic conductor RbAg_4I_5 using atomic force microscopy. *Applied Physics Letters* (2004), 3552-3555.
- [11] S. Shi, J. Sun, G. Zhang, J. Guo, Z. Wang, The growth of thin silver nanowires bundle using RbAg_4I_5 crystal grain thin film and the ionic conductivity of the thin film. *Physica B* (2005), 266–270.
- [12] X. Liang, Y. Chen, L. Chen, J. Yin, Z. G. Liu, Electric switching and memory devices made from RbAg_4I_5 films. *Applied Physics Letters* (2007), 022508.
- [13] X. Guo, C. Schindler, S. Menzel, R. Waser, Understanding the switching-off mechanism in Ag^+ migration based resistively switching model systems. *Applied Physics Letters*, (2007), 133513-133516.
- [14] X. F. Liang, Y. Chen, B. Yang, J. Yin, Z. G. Liu, A nanoscale nonvolatile memory device made from RbAg_4I_5 solid electrolyte grown on a Si substrate. *Microelectronic Engineering*, (2008), 1736–1738.
- [15] Q. Lai, L. Zhiyong, L. Zhang, L. Xuema, W. F. Stickle, Z. Zhu, Z. Gu, T. I. Kamins, R. S. Williams, Y. Chen, An Organic / Si Nanowire Hybrid Field Configurable Transistor 2008. *Nano Letters* (2008), 1–5.

- [16] V. P. Kuznetsov, M. E. Kompan, Capacitance Characteristics of Nanoporous Carbon Materials in Ionistors Based on RbAg_4I_5 Solid Electrolyte. *Russian Journal of Electrochemistry*, (2009), 574–577.
- [17] I. Valov, I. Sapezanskaia, A. Nayak, T. Tsuruoka, T. Bredow, G. Staikov, M. Aono, R. Waser, Atomically controlled electrochemical nucleation at superionic solid electrolyte surfaces. *Nature Materials*, (2012), 530–535.
- [18] I. Valov, M. N. Kozicki, Cation-based resistance change memory. *Journal of Physics D: Applied Physics*, (2013), 074005.
- [19] C. Escher, S. Thomann, C. Andreoli, H. Fink, J. Toquant, D.W. Pohl, Vacuum ion emission from solid electrolytes: An alternative source. *Applied Physics Letters*, (2006), 053513-053515.
- [20] M. Nishioka, H. Nanjyo, S. Hamakawa, K. Kobayashi, K. Sato, T. Inoue, F. Mizukami, M. Sadakata, O^- emission from $12\text{CaO} \cdot 7\text{Al}_2\text{O}_3$ and MSZ composite and its application for silicon oxidation. *Solid State Ionics* (2006), 2235–2239.
- [21] L. Bischoff, Application of mass-separated focused ion beams in nano-technology. *Nuclear Inst. and Methods in Physics Research, B*, (2008), 1846–1851.
- [22] G. R. Friedrich, Field emission devices for space applications. *Surface and Interface Analysis*, (2007), 116–122.
- [23] D. Pohl, H. Fink, J. Toquant, C. Escher, S. Thomann, C. Andreoli, High Brightness Solid State Ion Beam Generator, its Use and Method for Making such a Generator. Patent Number US20090121148 A1, University of Basel, University of Zuerich, (2006).
- [24] P. P. Kumar, S. Yashonath, Ionic conduction in the solid state. *Journal of Chemical Sciences*, (2006), 135–154.
- [25] http://2012books.lardbucket.org/books/general-chemistry-principles-patterns-and-applications-v1.0/section_16_04.html (June 2013).
- [26] S. Geller, *Solid Electrolytes-Topics in Applied Physics*, Springer-Verlag, Berlin Heidelberg, 1977.
- [27] M. J. Rice, W. L. Roth, Ionic transport in super ionic conductors: a theoretical model. *Journal of Solid State Chemistry* (1972), 294–310.
- [28] C. Escher, T. Latychevskaia, H. Fink, D. W. Pohl, Direct Evidence for Conduction Pathways in a Solid Electrolyte. *Physical Review Letters*, (2006), 136601-136604.
- [29] F. A. Karamov, *Superionic Conductors*, Cambridge International Science Publishing Ltd, 2008.
- [30] A. V. Boris, S. I. Bredikhin, Interface Charge Transport and Electronic Conductivity of RbAg_4I_5 Solid Electrolytes. *Solid State Ionics*, (1990), 269–271.
- [31] W. V. Johnston, Heat Capacity, Transformations, and Thermal Disorder in the Solid Electrolyte RbAg_4I_5 . *The Journal of Chemical Physics*, (1969), 3739–3747.
- [32] S. Geller, Low temperature phases of the solid electrolyte RbAg_4I_5 . *Physical Review B*, (1976), 4345–4355.

- [33] S. Hull, D. A. Keen, D. S. Sivia, P. Berastegui, Crystal Structures and Ionic Conductivities of Ternary Derivatives of the Silver and Copper Monohalides. *Journal of Solid State Chemistry*, (2002), 363–371.
- [34] C. H. J. Stuhrmann, H. Kreiterling, K. Funke, Ionic Hall effect measured in rubidium silver iodide. *Solid State Ionics*, (2002), 109–112.
- [35] D. Brinkmann, H. Arend, J. Roos, Evidence for a first-order transition at 209 K in the superionic conductor RbAg_4I_5 . *Solid State Communications*, (1978), 133–135.
- [36] R. A. Vargas, G. W. Coronel, First-order behaviour of the 209 K phase transition of RbAg_4I_5 . *Solid State Ionics*, (1995), 69–72.
- [37] S. Geller, Low temperature phases of the solid electrolyte RbAg_4I_5 . *Physical Review B*, (1976), 4345–4355.
- [38] K. Funke, R. D. Banhatti, D. Wilmer, R. Dinnebier, A. Fitch, M. Jansen, Low-Temperature Phases of Rubidium Silver Iodide: Crystal Structures and Dynamics of the Mobile Silver Ions. *The Journal of Physical Chemistry A*, (2006), 3010–3016.
- [39] A. R West, *Solid State Chemistry and its Applications*, John Wiley & Sons Ltd, Great Britain, 1992.
- [40] G. Staikov, E. Budevski, W. J. Lorenz, W. Wiesbeck, Frequency dispersion of the ionic conductivity of RbAg_4I_5 at low temperatures. *Solid State Ionics*, (1999), 101–108.
- [41] O. M. Shabanov, R. T. Kachaev, L. Kazievaa, High-voltage conductivity of $\alpha\text{-RbAg}_4\text{I}_5$, $\alpha\text{-KAg}_4\text{I}_5$ and $\alpha\text{-KCu}_4\text{I}_5$ superionic conductors. *Technical Physics*, (2012), 1157–1161.
- [42] B. Yang, X. F. Liang, H. X. Guo, K. B. Yin, J. Yin, Z. G. Liu, Characterization of RbAg_4I_5 films by pulsed laser deposition. *Journal of Physics D: Applied Physics* (2008), 115304.
- [43] Y. Cao, H. Sun, J. Sun, G. Tian, Z. Xing, J. Guo, Preparation and Structural Characterization of Superionic Conductor RbAg_4I_5 Crystalline Grain Films, *Chinese Letter of Physics*, (2003), 756-758.
- [44] H. Wang, L. Pilon, Interpretation of cyclic voltammetry for measuring electric double layer capacitances. *Electrochimica Acta*, (2012), 130–139.
- [45] T.T. Tsong, *Atom-Probe Field Ion Microscopy*, Cambridge University Press, Cambridge, 2005.
- [46] I. Guerrero, R. Bocanegra, F. J. Higuera, J. F. De La Mora, Ion evaporation from Taylor cones of propylene carbonate mixed with ionic liquids. *Journal of Fluid Mechanics*, (2007), 437–459.
- [47] P. Lozano, B. Glass, M. Martinez-Sanchez, Performance Characteristics of a Linear Ionic Liquid Electrospray Thruster. *29th International Electric Propulsion Conference*, Princeton University, (2005).
- [48] I. Romero-Sanz, R. Bocanegra, J. Fernandez de la Mora, M. , Source of heavy molecular ions based on Taylor cones of ionic liquids operating in the pure ion evaporation regime. *Journal of Applied Physics*, (2003), 3599-3606.

- [49] D. N. Zurlev, R. G. Forbes, Field ion emission: the effect of electrostatic field energy on the prediction of evaporation field and charge state. *Journal of Physics D: Applied Physics*, (2003), 74-78.
- [50] A. M. Belu, D. J. Graham, D. G. Castner, Time-of-flight secondary ion mass spectrometry: techniques and applications for the characterization of biomaterial surfaces. *Biomaterials*, (2003), 3635–3653.
- [51] A. Tolstogouzov, O. M. N. D. Teodoro, A. Santos, A. M. C. Moutinho, C. A. A. Ghumman, An upgraded TOF-SIMS VG Ionex IX23LS: Study on the negative secondary ion emission of III – V compound semiconductors with prior neutral cesium deposition. *Applied Surface Science*, (2012), 2490–2497.
- [52] R. G. Wilson, SIMS quantification in Si, GaAs, and diamond- an update, *International Journal of Mass Spectrometry and Ion Processes*, (1995), 43-49.
- [53] P. J. Wilbur, M. Wilson, K. Hutchings, The Emissive Membrane Ion Thruster Concept. *29th International Electric Propulsion Conference*, Princeton University, (2005).
- [54] C. M. Marrese-Reading, J.E Polk, J. Mueller, Spacecraft Propulsion applications for field emission cathodes, Jet propulsion laboratory, California Institute of Technology, (2001).